J. Fluid Mech. (2002), *vol.* 465, *pp.* 59–97.
DOI: 10.1017/S0022112002008947 Printed in the United Kingdom

The transition from steady to weakly turbulent flow in a close-packed ordered array of spheres

By REGHAN J. HILL AND DONALD L. KOCH

School of Chemical Engineering, Cornell University, Ithaca, NY 14853, USA

(Received 14 September 2000 and in revised form 11 February 2002)

The sequence of transitions in going from steady to unsteady chaotic flow in a close-packed face-centred cubic array of spheres is examined using lattice-Boltzmann simulations. The transition to unsteady flow occurs via a supercritical Hopf bifurcation in which only the streamwise component of the spatially averaged velocity fluctuates and certain reflectional symmetries are broken. At larger Reynolds numbers, the cross-stream components of the spatially averaged velocity fluctuate with frequencies that are incommensurate with those of the streamwise component. This transition is accompanied by the breaking of rotational symmetries that persisted through the Hopf bifurcation. The resulting trajectories in the spatially averaged velocity phase space are quasi-periodic. At larger Reynolds numbers, the fluctuations are chaotic, having continuous frequency spectra with no easily identified fundamental frequencies. Visualizations of the unsteady flows in various dynamic states show that vortices are produced in which the velocity and vorticity are closely aligned. With increasing Reynolds number, the geometrical structure of the flow changes from one that is dominated by extension and shear to one in which the streamlines are helical. A mechanism for the dynamics is proposed in which energy is transferred to smaller scales by the dynamic interaction of vortices sustained by the underlying time-averaged flow.

1. Introduction

The transition from steady to unsteady flow in porous media and the ensuing dynamics are not well understood because fluid flow in most porous media is extremely difficult to visualize and measure at the microscale. The length scales are typically of the order of or smaller than diagnostic probes, such as hot-wire anemometers. Furthermore, the presence of the solid makes it difficult to visualize such flows using quantitative optical techniques (Dybbs & Edwards 1984).

For unsteady flows in the presence of a steady applied pressure gradient, the flow is typically referred to as turbulent, even when the Reynolds number is relatively small. References to turbulent flow (Kaviany 1995) are motivated by observations of microscale hydrodynamic dispersion – typically a dye tracer – occurring in the small gaps between the particles (Jolls & Hanratty 1966; Dybbs & Edwards 1984). Even in steady flows, fluid elements undergo chaotic trajectories if the porous medium has a random structure. If temporal fluctuations from finite-Reynolds-number instabilities at the microscale give rise to periodic temporal fluctuations, these manifest as random fluctuations at macroscopic scales, since the temporal fluctuations are most likely to occur over a large volume and out of phase with one another. Therefore, when attempting to visually identify turbulent flow in random porous media, care must

be taken to determine the smallest length scale over which the apparently turbulent dispersion occurs. Long-range coupling is unlikely, because hydrodynamic interactions in random porous media are rapidly attenuated at separations larger than a few particle diameters. In ordered porous media, long-range order can be broken by the onset of unsteady flow (Hill & Koch 2002).

For steady flows in ordered and random arrays of spheres, the flow topology at moderate Reynolds numbers depends very much on the sphere configuration (Hill, Koch & Ladd 2001*b*). The dynamics of flows in three-dimensional geometries are likely to be different from those in two-dimensional arrays (Ghaddar 1995; Koch & Ladd 1997; Hill & Koch 2002) because, in addition to diffusion and convection of vorticity, three-dimensional flows admit the production of vorticity by vortex stretching. This enables kinetic energy at larger scales to be transferred to smaller scales, producing small-scale dissipative structures. Such an energy cascade might be used to distinguish low-Reynolds-number turbulence in porous media from unsteady laminar flow.

Pointwise velocity measurements have been made in porous media composed of ordered arrays of relatively large spherical particles. Mickley, Smith & Korchak (1965) and van der Merwe & Gauvin (1971) used hot-wire anemometer probes to measure turbulence statistics of flows in close-packed rhombohedral and simple-cubic arrays of spheres, respectively. Interpreting these measurements is particularly difficult, because the velocity fluctuations are anisotropic and their amplitude is comparable to the mean velocity – turbulence intensities in the approximate range 0.2–0.5 were reported. Consequently, the Taylor hypothesis is invalid and the spatial scales cannot be measured accurately from time series obtained at a fixed position. Unfortunately, comparisons of their results cannot be made with simulations, because the $O(10^3)$ Reynolds numbers considered are beyond the $O(10^2)$ values accessible with present computational resources.

Lebon *et al.* (1996) and Kutsovsky *et al.* (1996) have used nuclear magnetic resonance (NMR) imaging to obtain probability distribution functions (PDFs) of the fluid velocity in randomly packed beds of spheres. In these works, the Reynolds numbers were sufficiently small for the flows to be steady, and the velocity PDFs were found to decay exponentially at large positive velocities. When the abscissae were scaled with the average velocity, the PDFs did not change significantly with increasing Reynolds number, since at these small Reynolds numbers the flow topology is insensitive to the Reynolds number (Hill *et al.* 2001*b*). The changes in flow topology that occur at larger Reynolds numbers should significantly affect transport processes and statistical characteristics of the velocity fields.

Recently, Reynolds, Reavell & Harral (2000) performed lattice-Boltzmann simulations examining the dynamics of flows in a close-packed face-centred cubic array of spheres, with the flow directed along the (1,1,1) direction of the array. They compared simulations and experiments of tracer dispersion, and from their simulations identified transitions from steady to periodic, quasi-periodic and chaotic dynamics occurring at Reynolds numbers less than approximately 26. These transitions occur at much lower Reynolds numbers than in this work where the flow is directed along the (1,0,0) axis. As they point out, the difference can explained by considering the different cross-sectional areas between the spheres in the flow direction.

In this work, the dynamics of moderate-Reynolds-number flows in a close-packed face-centred cubic array of spheres are examined in detail. This geometry was chosen because experiments could, in principle, be performed to compare with simulations. Indeed, Wegner, Karabelas & Hanratty (1971) and Karabelas, Wegner & Hanratty

(1973) have examined the flow close to the surfaces of the spheres in such a configuration. They were particularly interested in the topology of the limiting streamlines and the velocity gradient at the surfaces, since the flow there plays an important role in heat and mass transfer. Away from the sphere surfaces, they noted that the streamlines emerging from four lobes on the downstream faces of the spheres spiral outward from their respective foci. Also of significance is the symmetry of the flow at the surface of the spheres – only one eighth of the surface needed to be examined. Their work focused on steady flows, partly because it is very difficult to observe the dispersion of a dye tracer when the flow is unsteady. Nevertheless, they noted that the transition to unsteady flow occurs at Reynolds numbers based on the sphere radius and the average velocity in the range 45–60. Unfortunately, they did not speculate on why the transitions to unsteady flow occurred over such a large range of Reynolds numbers.

The dynamics observed in an experiment, which necessarily has imperfections in the geometry that, for example, could break symmetries of the otherwise ordered microstructure, might be qualitatively different to those obtained from computations or theory that enforce such symmetries exactly. Indeed, Lahbabi & Chang (1985) studied the transition to unsteady flow in a close-packed simple cubic array of spheres, when the average velocity is directed along the primary axis of symmetry. Instead of solving the Navier–Stokes equations directly, they derived a low-dimensional model by projecting the Navier–Stokes equations onto basis functions (with up to five modes) that preserved many of the symmetries of the underlying geometry. While they observed physically plausible dynamics – a sequence of period doubling leading to chaotic flow – the dependence of the drag force on the Reynolds number was later found to be inaccurate (Ladd 1994*b*).

An interesting question to address then is whether the dynamics can be accurately reproduced when the symmetries imposed by the geometry are perturbed. In this work, symmetries are broken by briefly perturbing the direction of the average pressure gradient away from the axis of symmetry. The velocity field is not restricted to a sub-domain of the cubic unit cell, but only by the triply periodic boundary conditions. Consequently, symmetry breaking gives rise to quasi-periodic rather than a period-doubling route to chaotic dynamics.

In the next section, the physical parameters and various statistics used to diagnose the simulation results are described. This is followed by a discussion of the computational method and its limitations at the highest Reynolds numbers. Next, the results are presented. These comprise bifurcation diagrams for the amplitude and frequency of the fluctuations in the spatially averaged velocity, as well as the dependence of the drag force on the Reynolds number. Time series, and their respective Fourier spectra, of the streamwise and cross-stream components of the spatially averaged velocity are examined to highlight the sequence of bifurcations that leads from steady to unsteady chaotic flow. Also examined are two-dimensional projections of the velocity field and a three-dimensional flow visualization. These, together with statistics of the velocity, vorticity and helicity, are used to examine the spatial and temporal velocity fluctuations, and to elucidate some geometrical characteristics of the flows at various Reynolds numbers. Finally, a summary of the results is given.

2. Simulation methodology

The porous medium considered in this work is a close-packed face-centred cubic array of impermeable spheres with a solid volume fraction

$$c = \tfrac{16}{3}\pi(a/L)^2, \tag{1}$$

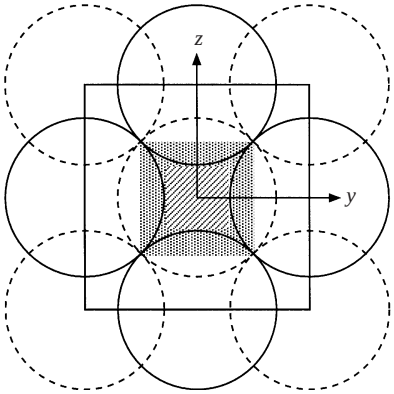

FIGURE 1. A projection of the close-packed face-centred cubic unit cell is shown within the outermost square, with the flow directed along the x-axis (out of the page). The solid and dotted lines identify spheres whose centres lie on planes whose unit normals are parallel to the x-axis, and the shaded areas highlight two cubic sub-domains used to examine the flows in later sections.

where a is the sphere radius and L is the size of the cubic computational domain, both measured in lattice units. In all the simulations considered in this work, the computational domain encloses four spheres whose centres coincide with the eight corners and the centres of the six faces of the triply periodic cubic domain.

Figure 1 shows the coordinate system and a projection of the unit cell onto the (y, z)-plane. Clearly, within the unit cell, the geometry is invariant to rotations of $\pi/2$ about the x-axis, and reflections about planes whose unit normals lie in the (y, z)-plane and are perpendicular to the lines $y = 0$, $z = 0$ and $y = \pm z$.

In this work, the applied body force is directed along the x-axis. This is convenient for performing simulations, since the average pressure gradient does not have to be obtained by trial-and-error to achieve a specified flow direction. It is also convenient for experiments, since the cubic array easily fits into a rectangular channel, which ensures that the spatially averaged velocity is directed along the primary axis of symmetry at all Reynolds numbers. Note that, at finite Reynolds numbers, there are no symmetries of the flow about any planes whose unit normals are parallel to the x-axis.

The velocity is considered as the sum

$$\boldsymbol{u}(\boldsymbol{x}, t) = \boldsymbol{U}(t) + \boldsymbol{u}'(\boldsymbol{x}, t), \tag{2}$$

where the spatially averaged velocity $\boldsymbol{U}$ is equivalent to the so-called *superficial* velocity measured in an experiment by dividing the volumetric flow rate by the cross-sectional area of the containing vessel. The average velocity in the space occupied by the fluid is simply $\boldsymbol{U}/(1 - c)$.

The Reynolds number is defined as

$$Re = \bar{U}_x a/\nu, \tag{3}$$

where ν is the fluid kinematic viscosity and the overbar indicates the time average.

The dimensionless drag force on the spheres is defined as

$$F = |\bar{\boldsymbol{f}}|/(6\pi\mu a|\bar{\boldsymbol{U}}|), \tag{4}$$

where μ is the fluid viscosity. Note that, since only one unit cell is considered, spatial periodicity requires that the drag force on all four spheres in the computational

domain be equal. Also, since the applied body force must balance the time-averaged drag force, the time-averaged drag force on the spheres is known *a priori*. It follows that, at steady state, the average drag force multiplied by the sphere number density is equal to the average pressure gradient, and hence the magnitude of the average pressure gradient is

$$|\langle \nabla p \rangle| = 9\mu c F |\bar{\boldsymbol{U}}|/(2a^2). \tag{5}$$

Because flows with chaotic fluctuations have a statistical uncertainty coming from the fluctuating spatially averaged velocity, the fundamental frequency, ω_1, is non-dimensionalized with the inverse of the viscous time scale, a^2/ν, rather than the convective time scale, $a/|\bar{\boldsymbol{U}}|$.

The amplitude of the fluctuations in the components of the spatially averaged velocity are characterized by the standard deviations of the components of the fluctuating spatially averaged velocity, non-dimensionalized with ν/a to give Reynolds numbers,

$$A_i = \overline{U_i' U_i'}^{1/2} a/\nu \quad (i = x, y, z), \tag{6}$$

where $U_i' = U_i - \bar{U}_i$. The fluctuations in the streamwise and cross-stream directions will be referred to as

$$A_\parallel = A_x \quad \text{and} \quad A_\perp = (A_y + A_z)/2, \tag{7}$$

respectively, since the y- and z-directions cannot, in general, be distinguished from one another, although in some cases this symmetry may be broken. Note that the amplitude of a sinusoidal oscillation with the same average fluctuating kinetic energy is $\sqrt{2}$ times larger than its standard deviation.

3. Computational checks

The pressure and fluid velocity are computed using the lattice-Boltzmann method of Ladd (1994*a*, *b*), which approximates solutions of the incompressible Navier–Stokes equations, with the no-slip boundary condition at the solid surfaces and periodic boundary conditions at the bounds of the computational domain. In addition to ensuring adequate spatial and temporal resolution, care must be taken when using the lattice-Boltzmann method to ensure that the velocity fields are not adversely affected by the fluid's compressibility (Hill & Koch 2002). This section quantitatively compares simulations with various grid resolutions and then addresses the effects of fluid compressibility.

To examine the effect of the grid resolution on the dynamics of the flows, simulations were performed with sphere radii of 19.8, 31.8 and 48.8 lattice units. The simulations with the largest sphere radius of 48.8 lattice units had 138^3 lattice nodes and were advanced by up to approximately 5×10^5 time steps. Table 1 compares various statistics obtained from these simulations at Reynolds numbers in the range where the flow undergoes transitions from periodic to chaotic dynamics and, hence, are most sensitive to the grid resolution. The simulations with similar Reynolds numbers, but with different sphere radii, have the same drag force, and hence the difference in the average velocities is because of the different grid resolutions and the slightly different solid volume fractions. The time series from which these statistics were obtained, and details of the dynamics, may be found in the thesis of Hill (2001).

As with previously published results for steady flows (Maier *et al.* 1998; Hill *et al.* 2001*b*), the non-dimensional drag force on the spheres is not very sensitive to the

a	c	$4f$	Re	F	$A_\parallel$	$A_\perp$	$\omega_1 \nu/a^2$	s/p/q/c
19.8	0.741	5000	37.0	747	0	0	∞	s
		6000[1]	42.2	786	0.585	0	103	p
		7000[1]	46.8	825	0.604	0	111	p
		9000[2]	(53.7) 53.8	(926) 924	0.0190	0	433	p
		11 000[3]	(60.8) 60.9	(1000) 998	0.0489	—	478	p
		13 000[4]	—	—	—	—	—	—
31.8	0.739	7000	(45.0) 45.8	(860) 845	0.563	0	116	p
		9000	(52.6) 53.4	(946) 931	0.505	0.138	116	q
		11 000	(59.5) 59.2	(1020) 1030	0.299	0	212	p
		13 000	(65.9) 65.5	(1090) 1100	0.386	0.232	230	c
48.8	0.741	7000[5]	45.7	847	0.699	0	122	p
		9000	(51.9) 53.1	(959) 936	0.622	0.319	135	c
		11 000	(58.8) 59.5	(1030) 1030	0.481	0.464	135	c
		13 000	(65.2) 65.0	(1100) 1110	0.448	0.367	229	c

TABLE 1. Comparison of simulations with grid resolutions corresponding to sphere radii of 19.8, 31.8 and 48.8 lattice units. In the range of Reynolds numbers considered here, the dynamics are the most difficult to capture accurately at long times because of the transition from periodic to chaotic flow. The results in brackets refer to the quasi-steady state that is typically approached before the growth of unstable modes if the fluid is accelerated from rest. Steady, periodic, quasi-periodic and chaotic states are denoted by the letters s, p, q and c respectively. [1]A quasi-steady solution was not approached. [2]Unphysical long-time behaviour. [3]Unbounded growth at long time. [4]Unbounded growth at short time. [5]Non-zero initial condition.

grid resolution, even in cases where the dynamics at long times are qualitatively different. In the range of Reynolds numbers where the flow undergoes a transition from periodic to chaotic behaviour, grid-independent dynamics are more difficult to capture. Nevertheless, the amplitudes and frequencies of the time series outside this range are in reasonable agreement. Unfortunately, a more comprehensive study that quantifies the effects of changing the grid resolution on the various statistics is beyond our computational resources. Most quantitative results presented in the following sections are from simulations with the largest sphere radius of 48.8 lattice units. While the results of simulations with a smaller sphere radius of 31.8 lattice units are usually in reasonable quantitative agreement, they are used more often for qualitative comparisons, such as flow visualization.

The local Mach number for the simulations with the largest Reynolds numbers may be high enough for the fluid's compressibility (which is not modelled exactly by this lattice-Boltzmann formulation) to adversely affect the results. Because the computational cost is approximately proportional to a^5, and our goal is to perform a parametric study, simulations with smaller Mach numbers – achieved by using even finer grids, for example – are beyond present resources. Nevertheless, to give a conservative indication of the Reynolds numbers above which compressibility artifacts may be expected, the maximum fluid velocity can be estimated from the velocity variances given in § 8. These suggest that the variance of the streamwise velocity fluctuations are at most $R_\parallel = 0.52$ times the square of the average fluid velocity inside the domain occupied by the fluid. Estimating the maximum velocity to be the mean plus four standard deviations gives a Mach number $M = (1+4\sqrt{R_\parallel})Re\,\nu/(ac_s(1-c))$. For $M < 0.2$, this requires $Re < 30$ for $a = 31.8$ lattice units, and $Re < 46$ for $a = 48.8$ lattice units. Clearly, the maximum Mach number based on these estimates

increases in proportion to the Reynolds number. At the largest Reynolds number of approximately 110, for example, the maximum Mach number for $a = 48.8$ lattice units is approximately 0.48. Unfortunately, the extent to which a Mach number of this size – in a very small region of the domain – affects the flows is beyond the scope and, indeed, the computational resources of this work, but, nevertheless, will be an important issue to address in future studies with higher grid resolutions and, hence, lower Mach numbers.

Regarding pressure wave oscillations, we note that the frequency of sound waves traversing the computational domain, whose length L is 90 lattice units, at the sound speed is approximately $\omega = c_s/L = 0.0079$. In this work, the fluid kinematic viscosity, ν, and the sound speed, c_s, scaled with the lattice-node separation and time step, are 0.01 and $1/\sqrt{2}$, respectively. With a sphere radius of 31.8 lattice units, the dimensionless frequency, $\omega a^2/\nu$, is 795. This is much higher than those of the underlying fluid velocity fluctuations, which are in the range 80–150 at Reynolds numbers in the range 30–60 (see figure 3). Clearly, the separation in time scales, between the underlying velocity fluctuations and the time for sound waves to propagate across the domain, makes it unlikely that the dynamics are dominated by those of spurious pressure oscillations. Furthermore, another test for the effect of sound waves on the dynamics is to vary the sphere radius and, hence, the size of the computational domain. As above, if we suppose that the frequency corresponding to sound waves traversing the computational domain is $O(c_s/L)$, then the non-dimensional frequency is $O(c_s a^2/(\nu L))$, which is is proportional to a when the solid volume fraction and other variables are fixed. However, as shown in table 1, more than doubling the sphere radius, from 19.8 to 48.8 lattice units, increases the non-dimensional fundamental frequency of the periodic fluctuations, at a Reynolds number of approximately 45, by less than 10%. Again, the dynamics are suggested to be dominated by those of the underlying incompressible fluid.

4. Bifurcations

In this section, the dependence upon the Reynolds number of: (i) the standard deviations of the fluctuating components of the spatially averaged velocity; (ii) the fundamental frequency of the fluctuating streamwise component of the spatially averaged velocity; and (iii) the time-averaged non-dimensional drag force are examined. These quantities help to characterize the underlying dynamics of the flows and the transitions that occur with increasing Reynolds number. Before presenting results that characterize the long-time behaviour, the initial transient is discussed briefly, since in many cases the long-time dynamics take a deceptively long time to fully develop.

If the fluid is first accelerated from rest by a constant average pressure gradient, the spatially averaged velocity undergoes a rapid transient, with a duration of less than approximately $0.025a^2/\nu$, causing it to briefly overshoot its long-time average value. If the Reynolds number is sufficiently large, the spatially averaged velocity typically relaxes to a quasi-steady or unstable steady state before developing temporal fluctuations at a later time. The development of these fluctuations is typically initiated by the growth of a mode that perturbs the cross-stream components of the spatially averaged velocity. At smaller Reynolds numbers, the spatially averaged velocity eventually develops periodic temporal fluctuations in only the streamwise component, whereas at larger Reynolds numbers, all three components fluctuate chaotically.

The time it takes for the long-time dynamics to develop decreases with increasing Reynolds number. At Reynolds numbers close to the critical value, Re_c, it takes

an $O(\sigma_1^{-1})$ time for the linearly unstable modes to fully develop from the steady base state, and hence it is impractical to examine the transition to unsteady flow by performing simulations with an initially stationary fluid. Here, σ_1, which approaches zero as the Reynolds number approaches Re_c from above, is the real part of the eigenvalue of the most unstable mode. To examine the Hopf bifurcation in detail, and hence to determine Re_c precisely, simulations were performed with initial velocity fields obtained from simulations with fully developed unsteady flows. At Reynolds numbers very close to Re_c, the mean and amplitude of the sinusoidally oscillating streamwise component of the spatially averaged velocity decayed exponentially toward their steady-state values, irrespective of the initial conditions. In such cases, the steady-state values could be obtained very accurately by fitting exponentially decaying functions to the time series over relatively short times. The frequency of the fluctuations during the transient period remained constant, as might be expected in the small range of Reynolds numbers where the dynamics are weakly nonlinear.

Simulations with a sphere radius of 48.8 lattice units were performed after examining the bifurcation diagrams obtained from simulations with a sphere radius of 31.8 lattice units. The results were similar, except in the intermediate range of Reynolds numbers where temporal fluctuations in the cross-stream components of the spatially averaged velocity develop. In this range of Reynolds numbers, the multiple solutions and hysteresis observed with a sphere radius of 31.8 lattice units ceased to exist with an increase in the grid resolution. Instead, the onset of temporal fluctuations in the cross-stream components of the average velocity was accompanied by a transition to quasi-periodic flow followed by the development of chaotic fluctuations at larger Reynolds numbers. As shown below, these bifurcations can be partially identified from the dependence of the amplitude of the fluctuating components of the spatially averaged velocity on the Reynolds number.

4.1. *Amplitude of the fluctuating spatially averaged velocity*

Figure 2 shows the dependence of $A_\parallel$ and $A_\perp$ on the Reynolds number obtained from simulations with a sphere radius of 48.8 lattice units. At a Reynolds number of approximately 30, the streamwise component of the spatially averaged velocity begins to oscillate sinusoidally with an amplitude of $\sqrt{2}A_\parallel$. The cross-stream components of the spatially averaged velocity begin to fluctuate at a Reynolds number of approximately 45. With increasing Reynolds number, the increasing amplitude of the fluctuating cross-stream components is accompanied by a decrease in the amplitude of the streamwise component. At Reynolds numbers in the approximate range 50–70, the amplitude of the fluctuations in all the components of the spatially averaged velocity are approximately equal. With a further increase in the Reynolds number, the amplitudes all increase at approximately the same rate. These fluctuations are chaotic, and the fluctuating kinetic energy is approximately equally partitioned amongst the streamwise and cross-stream directions. The dynamics of the spatially averaged velocity are coupled to the small-scale velocity fluctuations whose topology and statistics will be examined in following sections.

The simulation results at Reynolds numbers less than approximately 45 are given to a good approximation by the fit

$$A_\parallel = 1.33(Re/26.1 - 1)^{1/2} - 0.418 \quad (28.7 < Re < 45), \tag{8}$$

which gives a critical Reynolds number of approximately 28.7. The amplitude does not increase with the square root of a small parameter $\epsilon = Re/Re_c - 1$. This is possibly related to the symmetry of the unstable base state from which the small-amplitude

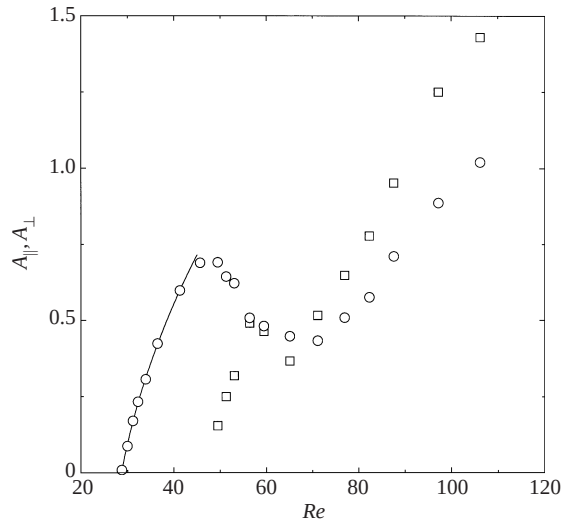

FIGURE 2. The characteristic amplitude of the streamwise (circles) and cross-stream (squares) components of the fluctuating spatially averaged velocity, non-dimensionalized with v/a, as a function of the Reynolds number. These results are from lattice-Boltzmann simulations with $(a, c) = (48.8, 0.741)$, where a is in lattice units. The line is a fit to the simulation results given by (8).

temporal fluctuations develop, and to the symmetries broken by the topological change that occurs with the onset of temporal fluctuations. If all the symmetries of the steady flow were forced upon the unsteady flow, then this might cause the constant on the right-hand side of (8) to vanish, which would give the square-root scaling typically expected for a supercritical Hopf bifurcation. The discontinuous changes in the rate at which $A_\parallel$ and $A_\perp$ increase with the Reynolds number, when $Re > 45$, can be attributed to further bifurcations, as will be seen when we examine the Fourier spectra of the time series.

4.2. *Frequency of the fluctuating spatially averaged velocity*

At Reynolds numbers between the critical Reynolds number and the Reynolds number where there first appear fluctuations in the cross-stream components of the spatially averaged velocity, there is an easily identified fundamental frequency in the time series of $A_\parallel$, which appears as an easily identified peak in the Fourier spectra. Figure 3 shows how the fundamental frequency increases with the Reynolds number over the range of Reynolds numbers where a fundamental frequency can be easily identified. Using the critical Reynolds number obtained from (8), the simulation results are given to a good approximation by the fit

$$\omega_1 a^2/\nu = 80.4 + 74.7(Re/28.7 - 1) - 8.94(Re/28.7 - 1)^2 \quad (28.7 < Re < 45). \qquad (9)$$

At the critical Reynolds number, the Strouhal number is $\omega_c a^2/(\nu Re_c) = 80.4/28.7 = 2.80$. In an experiment with water as the fluid, and with spheres whose radius is 2 cm, the frequency at the critical Reynolds number would be approximately $80.4\nu/a^2 = 0.2$ Hz. At larger Reynolds numbers, there are an increasing number of commensurate and incommensurate frequencies that appear in the Fourier spectra.

4.3. *Drag force*

Figure 4 shows the dependence of the non-dimensional drag force on the Reynolds number. At Reynolds numbers beyond the small range where the inertial correction

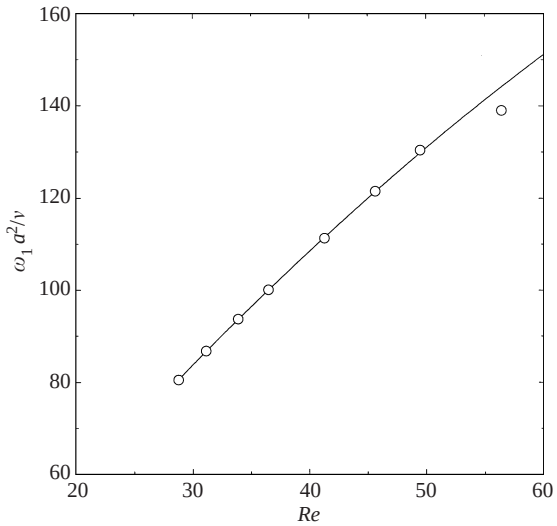

FIGURE 3. The fundamental frequency of the streamwise component of the fluctuating spatially averaged velocity, non-dimensionalized with ν/a^2, as a function of the Reynolds number. These results are from lattice-Boltzmann simulations with $(a, c) = (48.8, 0.741)$. The line is a fit to the simulation results given by (9).

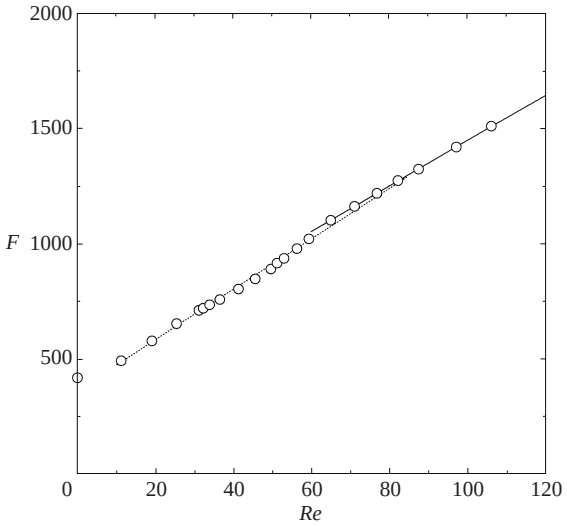

FIGURE 4. The non-dimensional drag force as a function of the Reynolds number from lattice-Boltzmann simulations with $(a, c) = (48.8, 0.741)$. The dotted and solid lines are linear fits to the simulation results, given by (10) and (11), respectively.

to $F(Re = 0)$ is actually proportional to Re^2 (Hill, Koch & Ladd 2001*a*), F increases approximately linearly with Re. The dotted and solid lines shown in figure 4 are the fits

$$F = 365 + 10.9Re \quad (10 < Re < 80), \tag{10}$$

and

$$F = 462 + 9.85Re \quad (Re > 80), \tag{11}$$

respectively.

Although (11) was fitted to the simulation results with $Re > 80$, it provides an excellent approximation for $Re > 60$. At smaller Reynolds numbers, the drag force does not increase exactly linearly with Re, because the flow topology changes as the flow undergoes the transition from steady to chaotic dynamics. Nevertheless, (10) provides a reasonable approximation to the data at Reynolds numbers where the dynamics are not yet 'fully developed', i.e. the time-averaged flow topology is not self-similar with increasing Reynolds number.

5. Dynamics of the spatially averaged velocity

The time series of the streamwise and cross-stream components of the spatially averaged velocity are shown in figures 5 and 6, respectively. These illustrate the qualitative changes that occur with the transition from periodic to chaotic dynamics. The components of the spatially averaged velocity are non-dimensionalized to give Reynolds numbers

$$Re_i = U_i a/\nu \quad (i = x, y, z). \tag{12}$$

The non-dimensional frequency corresponding to the sampling rate of the time series is approximately 4800, and hence, over the frequency ranges shown here, the accuracy of the spectra shown in figure 7 is limited by the time over which the time series were obtained. Nevertheless, the length of the time series was usually sufficiently long to resolve frequencies down to $10\nu/a^2$.

In general, at smaller Reynolds numbers, the fluctuations in the cross-stream components of the spatially averaged velocity are sufficiently small that they do not affect those in the streamwise direction. Compare, for example, the time series of the streamwise component of the spatially averaged velocities in figure 5(*a–c*) with the respective time series of the cross-stream components in figure 6. At larger Reynolds numbers, the fluctuating streamwise component of the spatially averaged velocity is influenced much more by the cross-stream components. This gives rise to relatively small-amplitude high-frequency fluctuations superposed on relatively large-amplitude low-frequency streamwise fluctuations. Compare, for example, the time series of the streamwise component of the spatially averaged velocity in figure 5(*e*) with the respective time series of the cross-stream components in figure 6.

Figure 5(*a*) shows the relaxation of the spatially averaged velocity from a simulation whose initial velocity field was obtained from a simulation with a fully developed unsteady flow at a larger Reynolds number. The flow rapidly develops approximately sinusoidal fluctuations in the streamwise component of the spatially averaged velocity. As shown in figure 6(*a*), the cross-stream components decay so there remain only fluctuations in the streamwise component at long times, which is also the case at smaller Reynolds numbers. Although they are not shown, the Fourier spectra of the fluctuating streamwise component of the spatially averaged velocity have peaks at the fundamental frequency, ω_1, and its higher frequency harmonics, $n\omega_1$ ($n = 2, 3, \ldots$).

Figure 5(*b*) shows the development of the quasi-periodic dynamics that occurs when the cross-stream components of the spatially averaged velocity first begin to fluctuate. The amplitude of the cross-stream components shown in figure 6(*b*) are modulated with the same low frequency as the streamwise component. The Fourier spectra of the streamwise and cross-stream components of the spatially averaged velocity are shown in figures 7(*a*) and 7(*b*), respectively. The streamwise component has a fundamental frequency of $\omega_1 \sim 130\nu/a^2$ and two higher frequency harmonics, $2\omega_1$ and $3\omega_1$. The cross-stream components have peaks in the spectra at frequencies that are, to the resolution achieved here, incommensurate with those of the streamwise component.

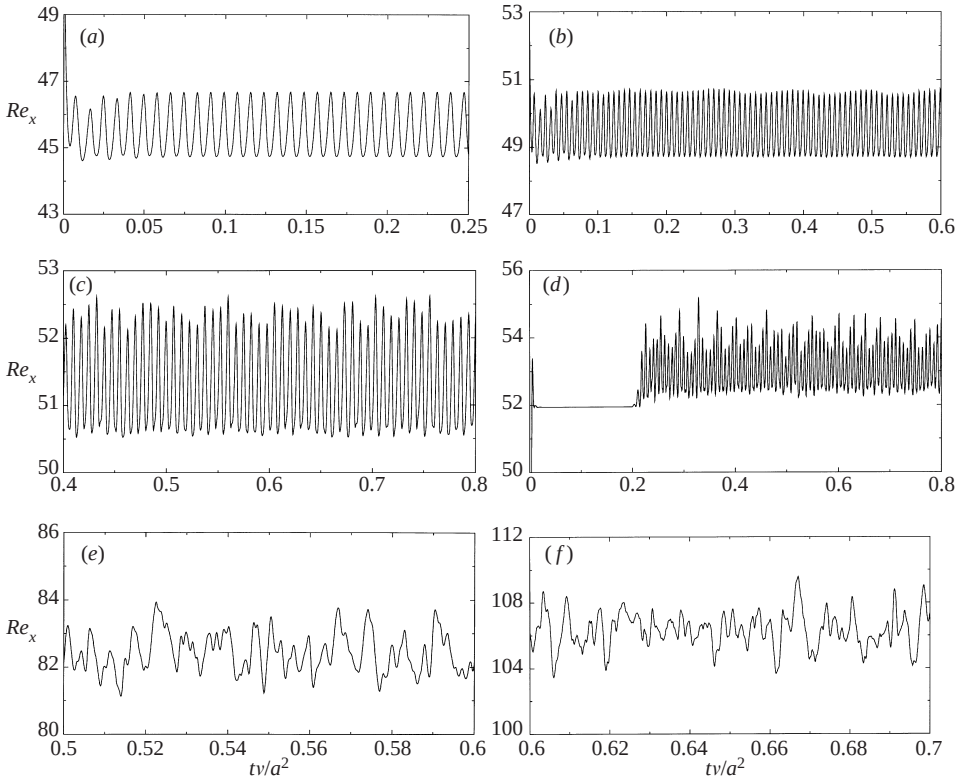

FIGURE 5. Time series of the x- (streamwise) component of the spatially averaged velocity, non-dimensionalized with v/a to give Reynolds numbers, from lattice-Boltzmann simulations with $(a, c) = (48.8, 0.741)$, where a is in lattice units. Time series of the corresponding cross-stream components are shown in figure 6. (a) $Re = 45.7$, (b) 49.5, (c) 51.3, (d) 53.1, (e) 82.4, (f) 106.2.

The 'satellite' peaks give rise to the amplitude modulation. It is interesting to note that the dynamics of the y- and z-components of the spatially averaged velocity are not the same, indicating a breaking of symmetry.

The Fourier spectra in figure 7 show that the route to chaos occurs via a transition to flow on a three-torus, rather than period-doubling as for two-dimensional ordered arrays of aligned cylinders (Koch & Ladd 1997; Hill & Koch 2002). At a Reynolds number of 49.5, the peaks in the Fourier spectra occur at frequencies that can be obtained from linear combinations of three fundamental frequencies, $\omega_1 = 130v/a^2$, $\omega_2 = 4.81v/a^2$ and $\omega_3 = 2.52v/a^2$. The peaks in the spectra for the x- and z-components of the spatially averaged velocity occur at frequencies given by $(m\omega_1 \pm n\omega_2)$, where m and n are positive integers. Those of the y-component occur at the same frequencies as the x- and z-components, but with a shift of ω_3 to slightly higher frequencies. The amplitudes of the peaks at these frequencies for each component are very different because of the breaking of symmetry in the (y, z)-plane. The fundamental frequency ω_1 dominates the fluctuating streamwise component of the spatially averaged velocity, whereas the frequencies ω_2 and ω_3 give rise to the modulated amplitude seen in figure 6(b).

The almost-periodic dynamics that occur at a Reynolds number of 49.5 give way to chaotic dynamics at an only slightly larger Reynolds number of 51.3. This is demonstrated by the continuous spectra shown in figure 7(b) and the time series

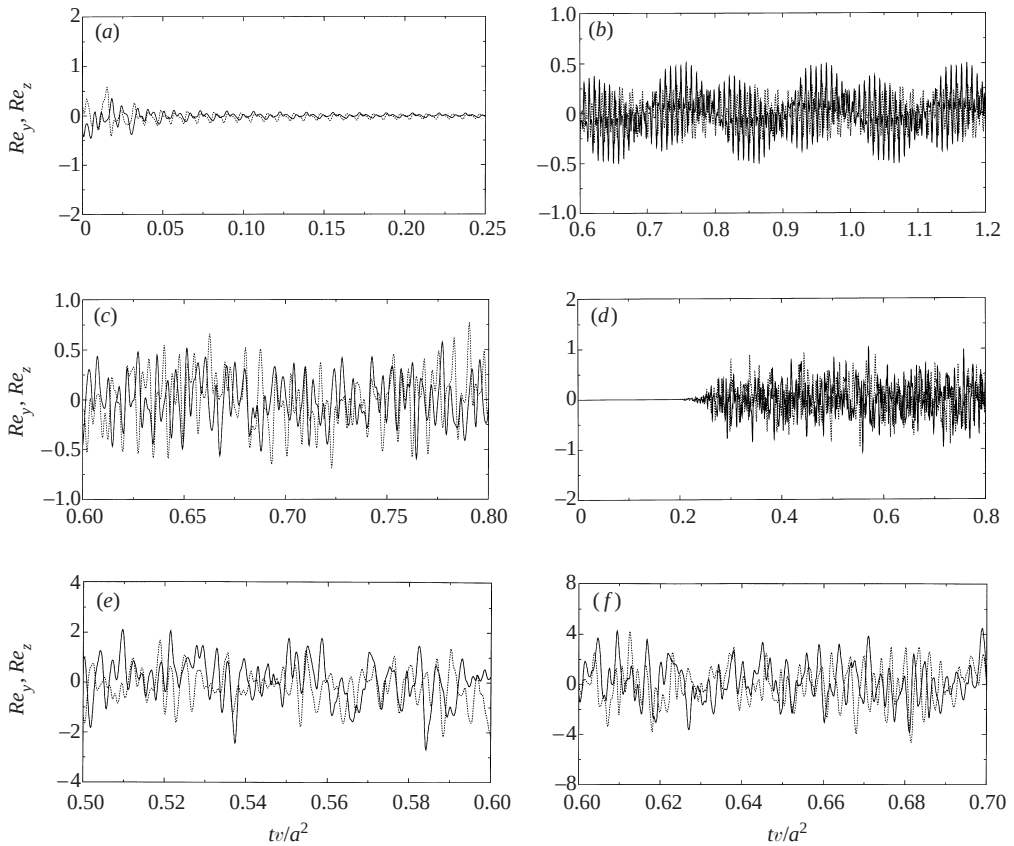

FIGURE 6. Time series of the y- (solid) and z- (dotted) components of the spatially averaged velocity, non-dimensionalized with v/a to give Reynolds numbers, from lattice-Boltzmann simulations with $(a, c) = (48.8, 0.741)$, where a is in lattice units. Time series of the corresponding streamwise components are shown in figure 5. (*a*) $Re = 45.7$, (*b*) 49.5, (*c*) 51.3, (*d*) 53.1, (*e*) 82.4, (*f*) 106.2.

shown in figures 5(*c*) and 6(*c*), for example. The transition to chaotic dynamics is accompanied by the time-averaged flow regaining the symmetry that was broken in the quasi-periodic regime at a Reynolds number of 49.5. With increasing Reynolds number, the density of distinct frequencies in both the streamwise and cross-stream directions increases considerably. At the largest Reynolds numbers considered, the peaks in the spectra are sufficiently numerous that they cannot be unambiguously distinguished from one another.

Despite the different times over which they are shown, the time series in figures 5(*d*) and 6(*d*) for a Reynolds number of 53.1 are qualitatively similar to those at a Reynolds number of 51.3. Also shown is the quasi-steady state that precedes the transition to chaotic unsteady flow. Although the dynamics appear to be evolving on a relatively long time scale, continuing this simulation to much longer times did not change the behaviour seen here. In all the simulations performed in this work, there was no evidence of intermittent transitions between chaotic and quasi-periodic or periodic flow.

Figures 5(*e*) and 5(*f*) show time series at Reynolds numbers where the Fourier spectra are continuous and their dominant peaks have broadened considerably. In both cases, the time series of the streamwise components have relatively small-amplitude high-frequency fluctuations superposed on relatively large-amplitude low-

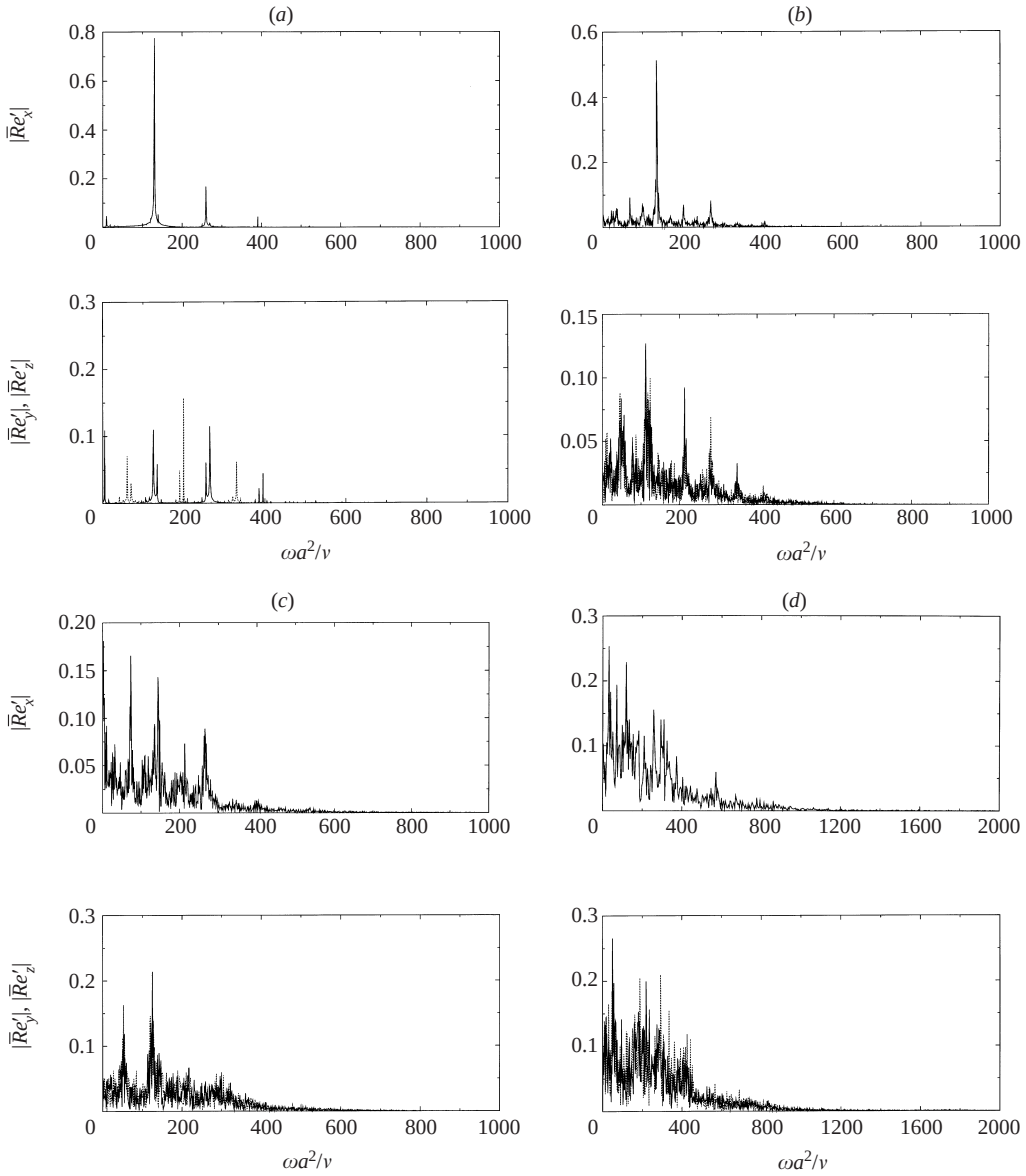

FIGURE 7. Fourier spectra of time series of the fluctuating streamwise (solid) and cross-stream (dotted) components of the spatially averaged velocity, non-dimensionalized with ν/a to give Reynolds numbers, from lattice-Boltzmann simulations with $(c, a) = (48.8, 0.741)$, where a is in lattice units. (*a*) $Re = 49.5$, (*b*) 53.1, (*c*) 59.5, (*d*) 82.4.

frequency fluctuations. The time series of the cross-stream components shown in figures 6(*e*) and 6(*f*) suggest that the high-frequency contributions to the streamwise components come from a much stronger interaction with the cross-stream components than at smaller Reynolds numbers. Indeed, as was shown in figure 2, the amplitudes of the streamwise and cross-stream components of the spatially averaged velocity are comparable at these Reynolds numbers.

The Fourier spectra of all the components of the spatially averaged velocity shown in figures 7(*c*) and 7(*d*) have a continuous distribution of frequencies. The distinct

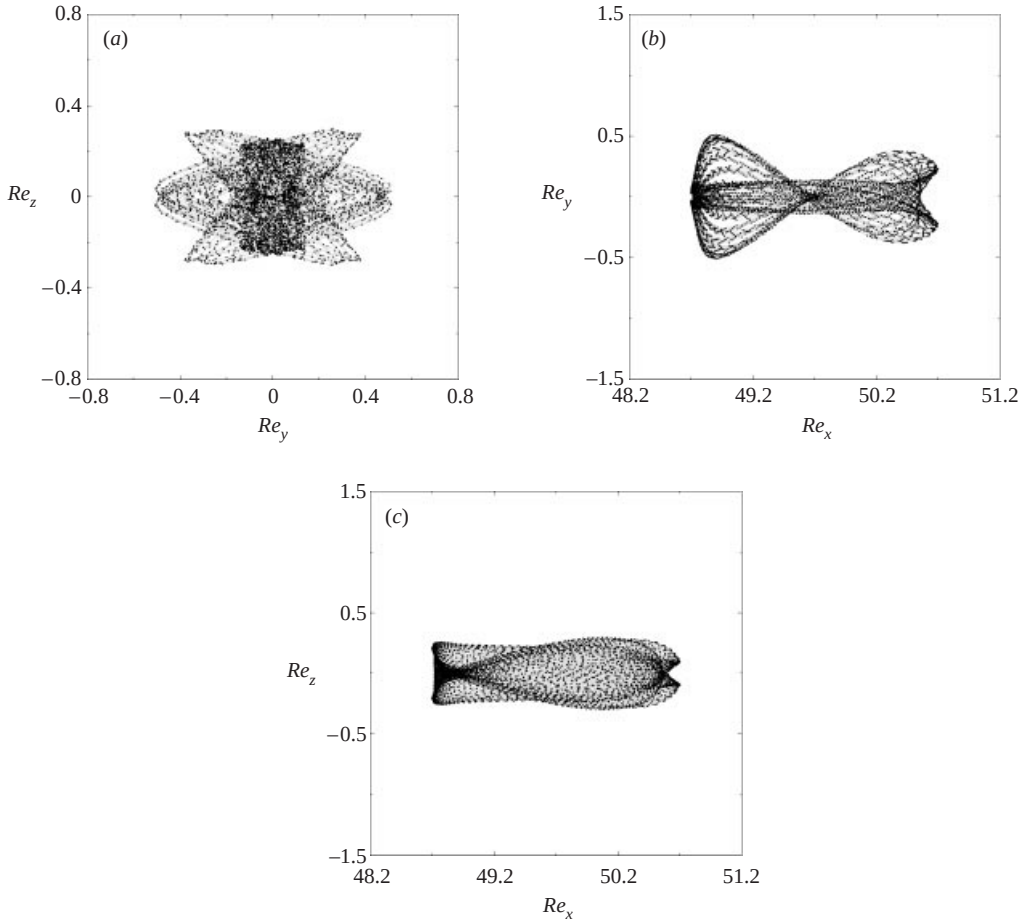

FIGURE 8. Projections of the spatially averaged velocity, non-dimensionalized with v/a to give Reynolds numbers, onto the (z, y)-, (y, x)- and (z, x)-planes. The points along the trajectories are separated by 50 time steps of a lattice-Boltzmann simulation with $(a, c) = (48.8, 0.741)$, where a is in lattice units.

peaks in the spectra of the streamwise component of the spatially averaged velocity at smaller Reynolds numbers have decreased in magnitude and broadened because the fluctuating kinetic energy is distributed amongst a larger number of modes. The dominant peaks in the spectra of the cross-stream components of the spatially averaged velocity have decreased in amplitude. At the largest Reynolds number, the fluctuating kinetic energy is distributed over a relatively wide range of frequencies. It is interesting to note that the qualitative differences between the spectra at these two Reynolds numbers could, perhaps, be attributed to one of the bifurcations suggested in §4.1 to give rise to the discontinuous change in the rates at which $A_\parallel$ and $A_\perp$ increase with Re at Reynolds numbers between 80 and 90 (see figure 2).

Figure 8 shows projections of quasi-periodic trajectories, in the phase space of the spatially averaged velocity, onto the (y, z)-, (x, y)- and (x, z)-planes in the corresponding velocity space. The manifold occupied by the trajectories clearly has a complicated structure, which is characterized by regular bursts in the amplitude of the cross-stream components. These, of course, can be easily identified in the time series shown in figures 5(b) and 6(b).

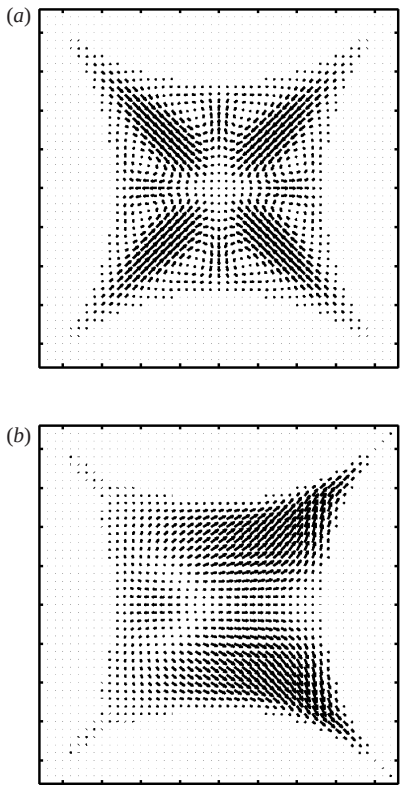

FIGURE 9. Projections of the fluid velocity onto the (y, z)- and (x, y)-planes. Only a subsection of the entire cross-sections are shown, since most of the region outside the views is occupied by the spheres. These results are from a lattice-Boltzmann simulation with $(Re, a, L, 4f) = (25.9, 31.8, 90, 3000)$, where a is in lattice units. At this Reynolds number, the flow is steady and has the same reflectional and rotational symmetries in the (y, z)-plane as the underlying geometry. The spatially averaged velocity in (a) is out of the page, whereas in (b) it is from left to right.

With increasing Reynolds number, the amplitude of the fluctuations in the cross-stream components of the spatially averaged velocity increase, and there develops a stronger coupling between the streamwise and cross-stream components. This coupling leads to the chaotic behaviour observed at larger Reynolds numbers, as can be seen in figure 6$(c–f)$, for example. When the dynamics become chaotic, the trajectories fill the entire space whose fluctuating kinetic energy is bounded by a constant that increases with the Reynolds number.

6. Flow topologies

While the spatially averaged velocity provides a useful quantitative means of interpreting the dynamics, averaging conceals many details. In this section, the topologies of the velocity fields are examined to highlight the symmetries of the flows at various Reynolds numbers, and to elucidate a mechanism for the self-sustained dynamics.

6.1. *Steady flow*

Figure 9 shows projections of the fluid velocity onto the (y, z)- and (x, y)-planes at a Reynolds number just below the critical value of 28.7. This is the steady base state from which unstable modes develop at larger Reynolds numbers. Clearly, the projection

of the velocity field in (*a*) has the same reflectional and rotational symmetries in the (y, z)-plane as the close-packed sphere configuration. A region of backward flowing fluid at the rear of the spheres and a region of slowly moving but non-recirculating flow at their upstream faces can be identified in figure 9(*b*). Together, the projections in (*a*) and (*b*) show that the steady base state could be computed using a sub-domain, with a triangular cross-section, whose volume is only 1/8th of the entire cubic domain. However, for the unsteady flows examined below, the flow rotates around the x-axis, and hence the entire computational domain is necessary.

It is interesting to note here the observations of Wegner *et al.* (1971), who performed experiments in which a dye tracer was released from various positions on the surface of a sphere embedded in such an array. They identified eight so-called focal points in the pattern of limiting streamlines on the downstream faces of the spheres. Also noted and photographed were eight helical trajectories issuing into the bulk flow. These observations provide convincing evidence that the simulations capture the correct flow topology, since there are, indeed, two rotating regions in each of the four corners of the projections shown in figure 9(*a*). These are presumably the cross-sections of eight vortex-like structures whose axes are aligned in the streamwise direction. The region of backward moving fluid at the downstream faces of the spheres shown in figure 9(*b*) is part of a recirculating flow that is similar to the annular vortex that forms in the wake of a single sphere in an unbounded fluid at moderate Reynolds numbers. However, in this flow it is considerably shorter and is partitioned into at least four, but possibly eight, sub-domains.

For comparison, figure 10 shows similar projections of the velocity field from a simulation with a Reynolds number of 106 and a sphere radius of 48.8 lattice units. This is the largest Reynolds number that was achieved in this work. While the chaotically fluctuating flow is significantly distorted from the steady base state shown above, similar large-scale features can still be identified.

6.2. *Periodically fluctuating flow*

With the onset of unsteady flow, the projection of the velocity field onto the (y, z)-plane loses its reflectional symmetry about the lines $y = \pm z$, but maintains its invariance to rotations of $\pi/2$ about the x-axis. This primary instability is followed by a secondary instability at larger Reynolds numbers that breaks all the symmetries of the flow in the (y, z)-plane, giving rise to quasi-periodic dynamics.

Periodic fluctuations in the spatially averaged velocity occur only in the streamwise direction. Based on only this information, one might be led to assume that the velocity field maintains the symmetries imposed by the geometry of the array. If this were the case, the fluid would pulse back-and-forward, similar to an axisymmetric mode of oscillation for a single sphere in an unbounded fluid. However, the projections of the velocity fields shown in figures 11 and 13 suggest that this is not the case. Instead, the fluid flowing along the x-axis alternates between clockwise and anticlockwise rotation around the x-axis.

The illustrations in figure 12 show a schematic of the flow projected onto the (y, z)-plane. Figure 12(*a*) highlights the symmetries of the steady base state from which periodic fluctuations develop. The sequence (*b–d*) illustrates the dynamics that occur during a fundamental period. The steady base state shown in (*a*) is perturbed by the generation of a vortex whose axis coincides with the x-axis. In this case, the vortex is shown, arbitrarily, with a clockwise rotation corresponding to positive vorticity. Note that the four pairs of vortices that exist in the steady base state are maintained by the inertia and viscous stresses generated by the 'jets' of fluid issuing from the

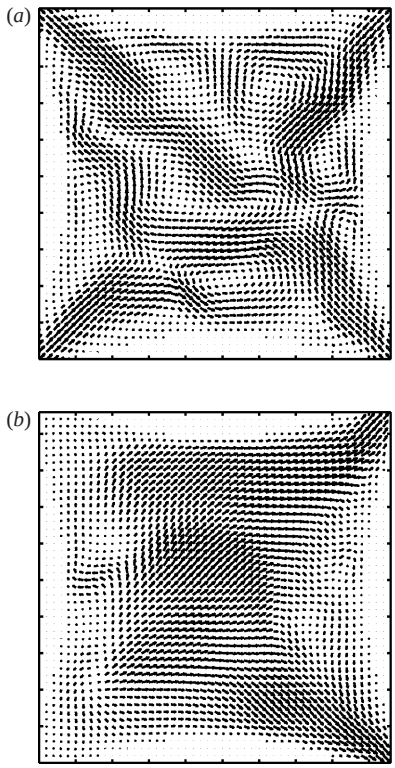

FIGURE 10. Projections of the fluid velocity onto the (y, z)- and (x, y)-planes. Only a small section of the cross-sections are shown, since most of the region outside the views is occupied by the spheres. These results are from a lattice-Boltzmann simulation with $(Re, a, L, 4f) = (106, 48.8, 138, 29\,000)$, where a is in lattice units. At this Reynolds number, the flow fluctuates chaotically and all the symmetries that were present at much smaller Reynolds numbers are broken. The spatially averaged velocity in (a) is out of the page, whereas in (b) it is from left to right.

four corners of the domain. These vortices persist throughout the cycle and play an important role in sustaining the unsteady motion.

One vortex in each of the four pairs, whose rotation is opposite to that of the vortex in the centre, is attracted toward the centre. The attraction can be rationalized by considering the interaction of a stationary line vortex with the velocity disturbance induced by the other vortex in the counter-rotating pair. In this scenario, the force on the fluid comes from the vortex term in the Navier–Stokes equations, $\boldsymbol{u} \times \boldsymbol{\omega}$ (Tennekes & Lumley 1994), which in this flow gives rise to an attraction of counter-rotating vortices. Consequently, the four vortices are swept toward the central vortex where they merge and coalesce under the influence of viscosity. After coalescing, the net rotation of the fluid is the same as at the beginning of the cycle, but its direction is reversed.

The projections of the velocity field onto the (x, y)-plane in figure 13 show that the periodic fluctuations are more subtle than at larger Reynolds numbers when all the components of the spatially averaged velocity fluctuate chaotically. The most significant change in the velocity fields can be seen by comparing the velocity vectors in the 5th and 8th images, for example. In the 5th image, the velocity is predominantly in the streamwise direction, whereas in the 8th image, the velocity in the top (bottom) half is predominantly upward (downward). These indicate that, similarly to the axial

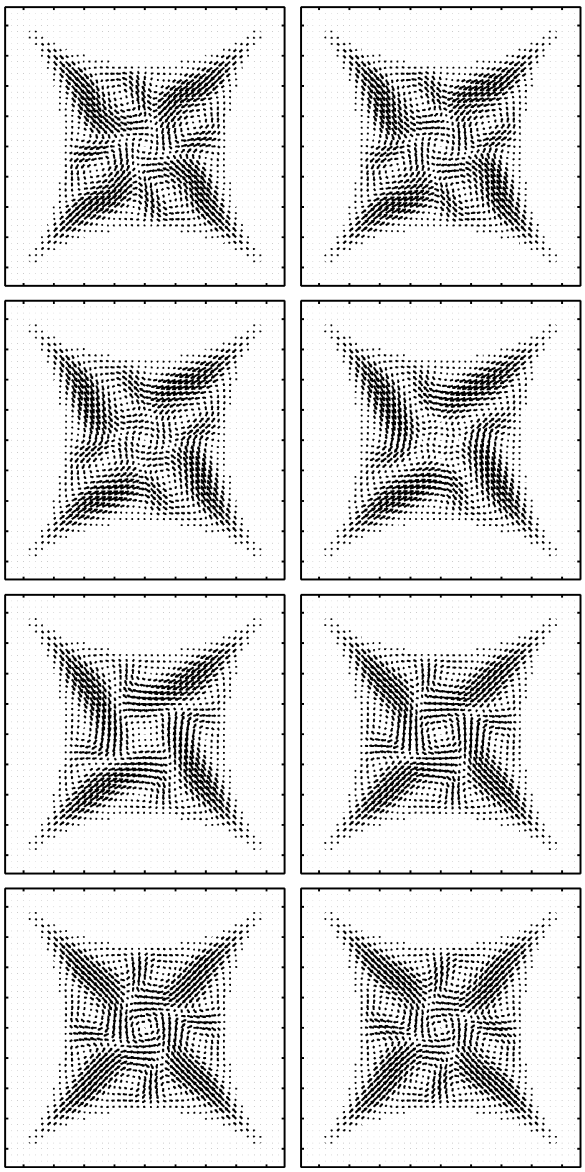

FIGURE 11. Projections of the fluid velocity onto the (y, z)-plane at equally spaced instants in time increasing from left to right and from top to bottom. Only a small subsection of the entire cross-section is shown, since most of the region outside the views is occupied by the spheres. In this figure, the spatially averaged velocity is directed out of the page and fluctuates periodically with a non-dimensional fundamental frequency $\omega_1 = 122\nu/a^2$. These results are from lattice-Boltzmann simulations with $(Re, a, c) = (47.7, 31.8, 0.739)$, where a is in lattice units, and the time between each snapshot of the flow, Δt, corresponds to $\Delta t\nu/a^2 = 9.89 \times 10^{-4}$.

compression and expansion of an elastic spring, the instantaneously helical streamlines undergo a cycle of contraction and expansion throughout the fundamental period.

6.3. *Chaotically fluctuating flow*

Figures 14–16 show a sequence of projections of the velocity field onto planes passing through the centre of the computational domain, at a Reynolds number

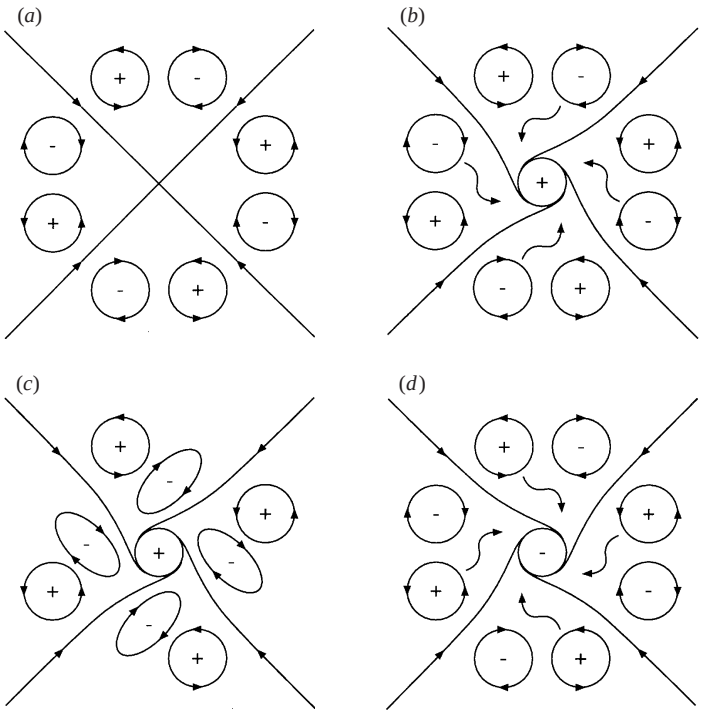

FIGURE 12. A schematic illustration of the mechanism for the symmetry-breaking instability that gives rise to periodic temporal velocity fluctuations. This sequence may be compared to the projections of the velocity field shown in figures 11 and 13. The plus and minus signs indicate the direction of rotation within the vortices identified with circles. The base state of the steady flow (*a*) (see figure 9) has no net rotation because of the invariance of the flow to rotations of $\pi/2$ about the x-axis. A perturbation giving rise to net rotation about the x-axis leads to an attractive force between vortices with opposite rotation (*b*). Merging and then coalescing (*c*) leads to a reversal of the net rotation about the x-axis (*d*).

where the spatially averaged velocity undergoes chaotic fluctuations. In contrast to the velocity fields shown in figures 13 and 11, whose streamwise component of the spatially averaged velocity fluctuates periodically, all symmetries are broken. Consequently, projections onto the (x, y)- and (x, z)-planes are shown in figures 15 and 16, respectively.

The axes of a pair of counter-rotating vortices attached to the upstream faces of the spheres can be seen to alternately align with the y- and z-axes. Because the geometry is invariant to rotations of $\pi/2$ about the x-axis, there is no reason for one orientation to be favoured over another. However, there must be sufficient energy to alternate between the two states. Recall that the quasi-periodic dynamics observed at a Reynolds number of 49.5 arbitrarily adopted one direction over the other, whereas at larger Reynolds numbers the time-averaged chaotic flow regains the previously broken symmetry, because the fluctuating cross-stream components of the velocity are sufficiently energetic.

The three-dimensional visualization in figure 17 highlights some of the vortical structures in the flow, particularly the pair of vortices that develops close to the upstream surface of the spheres, i.e. behind the sphere whose upstream facing surface is closest to the front of the sub-domains shown here (see figure 1). The 'ribbons' show trajectories in the instantaneous velocity fields; the light and dark trajectories

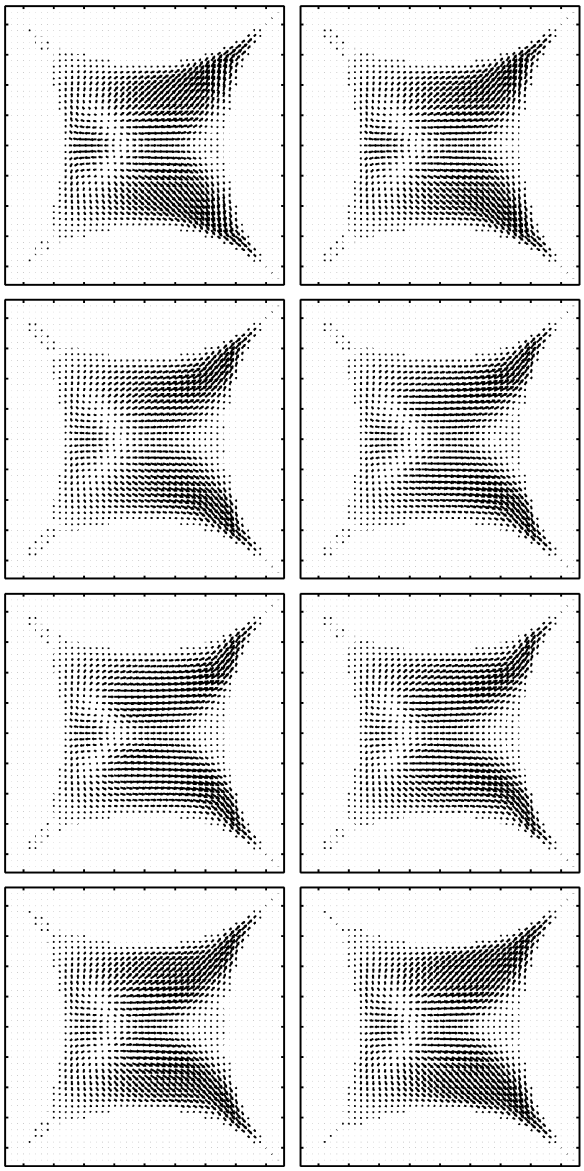

FIGURE 13. Projections of the same velocity fields shown in figure 11, but onto the (x, y)-plane.

are intended to help distinguish nearby trajectories. Iso-contours of the vorticity and velocity are shown by the light and dark surfaces, respectively. The magnitude of the vorticity or velocity on these surfaces is equal to its mean plus 1.75 times its standard deviation on the sub-domain shown. Clearly, the spaces occupied by helical streamlines often coincide with regions bounded by the surfaces of high vorticity. Furthermore, the highest velocities occur in the narrow gaps between the spheres, which are close to the corners of the cubic sub-domain shown here.

A mechanism for the evolution of the counter-rotating pairs of vortices is elusive, but one possibility is that they originate from an instability of the streamwise vortices characterizing the periodically fluctuating flows. Such an instability can be rationalized

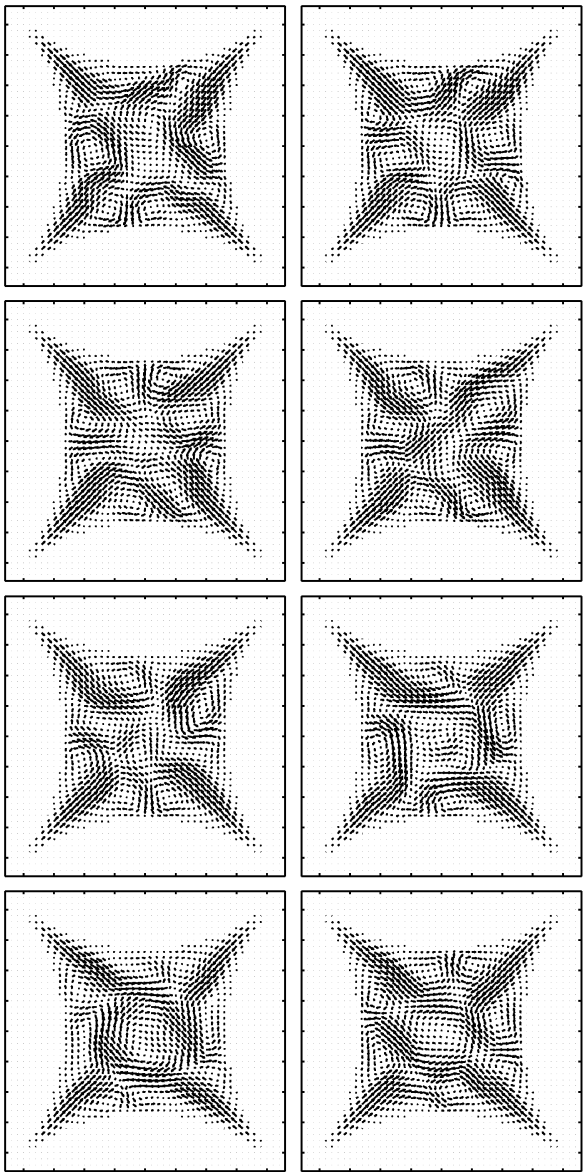

FIGURE 14. Projections of the fluid velocity onto the (y, z)-plane at equally spaced instants in time increasing from left to right and from top to bottom. Only a subsection of the entire cross-section is shown, since most of the region outside the views is occupied by the spheres. In this figure, the spatially averaged velocity is directed out of the page and fluctuates chaotically. These results are from lattice-Boltzmann simulations with $(Re, a, c) = (82.4, 31.8, 0.739)$, where a is in lattice units, and the time between each snapshot of the flow, Δt, corresponds to $\Delta t\nu/a^2 = 4.94 \times 10^{-4}$.

by considering a line vortex whose axis is aligned with the flow direction. In the absence of viscous stresses, any perturbation from a straight line leads to the growth of three-dimensional disturbances because of the force coming from the vortex term, $\boldsymbol{u} \times \boldsymbol{\omega}$, in the Navier–Stokes equations (Tennekes & Lumley 1994). The stretching of the vortex line that necessarily accompanies such a perturbation will intensify the vorticity, because of the stretching term, $\boldsymbol{\omega} \cdot \nabla \boldsymbol{u}$, in the vorticity conservation equation,

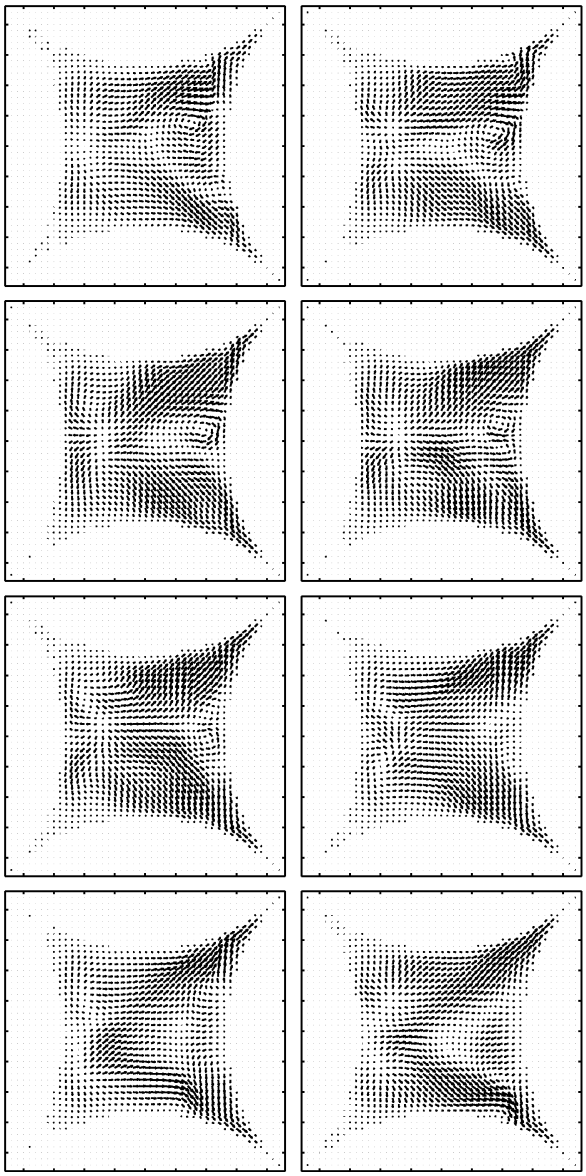

FIGURE 15. Projections of the same velocity fields shown in figure 14, but onto the (x, y)-plane.

and further increase the destabilizing force. A similar mechanism is known to produce omega-shaped vortices in turbulent boundary layers (Hinze 1987). The stretching of the vortices originally parallel to the flow would then be followed by rotation and convection downstream, possibly assisted by the large fluctuations in the velocity that cause streamlines originating from one quadrant to exit at another.

7. Spatial and temporal velocity fluctuations

In this section, the spatial velocity variance and its temporal evolution are used to quantitatively examine the spatial and temporal velocity fluctuations. This analysis

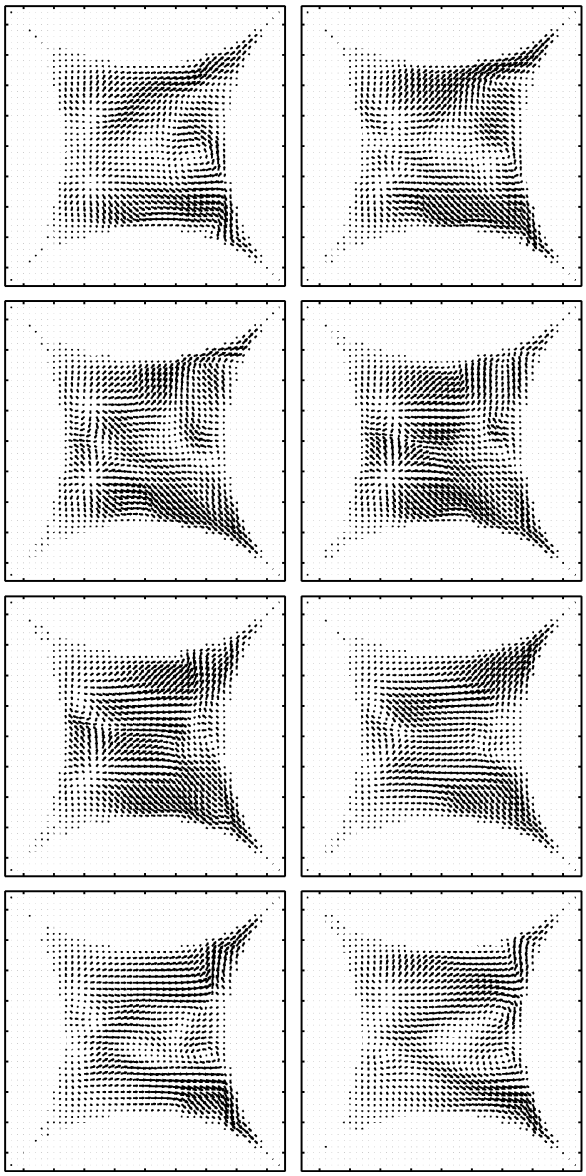

FIGURE 16. Projections of the same velocity fields shown in figure 14, but onto the (x, z)-plane.

shows that the temporal velocity fluctuations are significantly larger than those of the spatially averaged velocity. The temporal evolution of the spatial velocity variance, at Reynolds numbers where the dynamics are periodic, reveal the origin of the higher frequency harmonics in the Fourier spectra of the spatially averaged velocity. This analysis also shows how kinetic energy is exchanged between the fluctuating spatially averaged velocity and the fluctuating spatial velocity variance.

The spatial velocity variance, non-dimensionalized with the magnitude of the spatially averaged velocity, is defined as

$$\boldsymbol{R}(t) = \langle \boldsymbol{u}'\boldsymbol{u}' \rangle / |\boldsymbol{U}|^2, \tag{13}$$

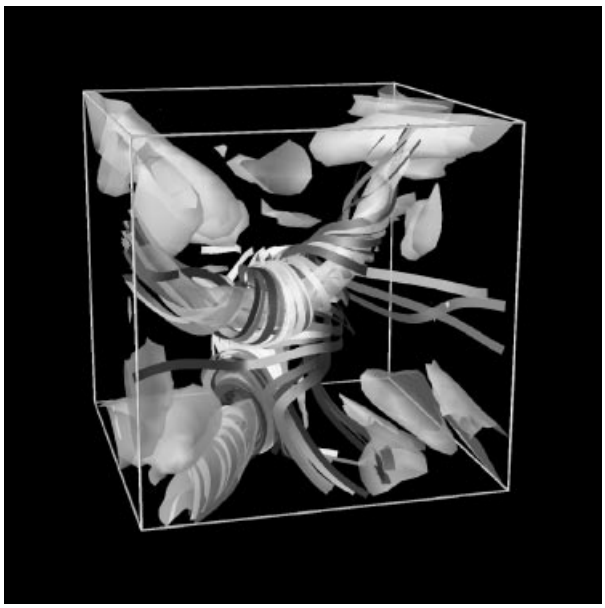

FIGURE 17. Trajectories in the velocity field, in the cubic sub-domain (see figure 1) whose sides are tangent to spheres at each face, at an instant in time coinciding with the third image in the sequence of projections of the velocity field shown in figures 14–16. The 'ribbons' highlight the vortical structures that evolve in the flow – they follow trajectories in the 'frozen' velocity fields. The dark and light surfaces are iso-contours of the magnitude of the velocity and vorticity, respectively. The views are off the (y, z)-plane, with the spatially averaged velocity directed out of the page.

where the angled brackets indicate the spatial average, which includes the space occupied by the spheres. The non-dimensional variance of the streamwise and cross-stream components of the velocity are given by the diagonal components of $\boldsymbol{R}$, which will be referred to as

$$R_{\parallel} = R_{xx} \quad \text{and} \quad R_{\perp} = (R_{yy} + R_{zz})/2, \tag{14}$$

respectively.

It is convenient to define characteristic velocities for the temporal velocity fluctuations in the streamwise and cross-stream directions by

$$V_{\parallel}^2 = 2\overline{(E_{\parallel} - \overline{E_{\parallel}})^2}^{1/2} \quad \text{and} \quad V_{\perp}^2 = 2\overline{(E_{\perp} - \overline{E_{\perp}})^2}^{1/2}, \tag{15}$$

respectively, where the overbars again indicate time averages and

$$E_{\parallel} = \tfrac{1}{2}|\boldsymbol{U}|^2(1 + R_{\parallel}) \quad \text{and} \quad E_{\perp} = \tfrac{1}{2}|\boldsymbol{U}|^2 R_{\perp} \tag{16}$$

are the contributions to the total kinetic energy, $E = E_{\parallel} + 2E_{\perp}$, from the streamwise and cross-stream components of the velocity.

Since the fluctuations in $|\boldsymbol{U}|$ are small compared to the mean, $V_{\parallel}/|\bar{\boldsymbol{U}}|$ and $V_{\perp}/|\bar{\boldsymbol{U}}|$ are approximately equal to the square root of the standard deviations, $\Delta_{\parallel}$ and $\Delta_{\perp}$, of the temporal fluctuations in $R_{\parallel}$ and $R_{\perp}$, respectively, i.e.

$$V_{\parallel}/|\bar{\boldsymbol{U}}| \sim \Delta_{\parallel}^{1/2} \quad \text{and} \quad V_{\perp}/|\bar{\boldsymbol{U}}| \sim \Delta_{\perp}^{1/2}, \tag{17}$$

Re	$4f$	$A_\parallel/Re$	$A_\perp/Re$	$\overline{R_\parallel}^{1/2}$	$\overline{R_\perp}^{1/2}$	$\Delta_\parallel^{1/2}$	$\Delta_\perp^{1/2}$	p/c
32.3	4150	0.0023	0	2.1	1.5	0.092	0.059	p
45.9	7000	0.012	0	2.1	1.5	0.22	0.14	p
83.0	19 000	0.0069	0.0072	2.1	1.5	0.30	0.25	c

TABLE 2. A comparison of spatial and temporal velocity fluctuations, from lattice-Boltzmann simulations with $(a, c) = (31.8, 0.739)$, where a is in lattice units. Time averages were obtained from snapshots of the velocity fields at approximately 10 equally spaced times throughout the fundamental period of the fluctuations. Recall, $A_\parallel$ and $A_\perp$ are the standard deviations of the streamwise and cross-stream components of the spatially averaged velocity, non-dimensionalized with v/a to give Reynolds numbers; $R_\parallel$ and $R_\perp$ are the variances of the streamwise and cross-stream components of the spatial velocity fluctuations, non-dimensionalized with the square of the magnitude of the spatially averaged velocity; and $\Delta_\parallel$ and $\Delta_\perp$ are the standard deviations of the temporal fluctuations in $R_\parallel$ and $R_\perp$, respectively. Periodic and chaotic dynamics are distinguished by the letters p and c, respectively.

where

$$\Delta_\parallel = \overline{(R_\parallel - \overline{R_\parallel})^2}^{1/2} \quad \text{and} \quad \Delta_\perp = \overline{(R_\perp - \overline{R_\perp})^2}^{1/2}. \tag{18}$$

Table 2 lists the results obtained from simulations with Reynolds numbers of approximately 32, 46 and 83, all with sphere radii of 31.8 lattice units. At these Reynolds numbers, the dynamics of the flows with this grid resolution are similar to those obtained from simulations with a sphere radius of 48.8 lattice units. Furthermore, the topology of the underlying velocity fields is practically the same, and, hence, the velocity variances are sufficiently accurate for the purpose of establishing the magnitude of the *local* temporal velocity fluctuations.

The local temporal velocity fluctuations are considerably larger than those of the spatially averaged velocity. Since the fluctuations in the spatially averaged velocity have been non-dimensionalized to give Reynolds numbers, $A_\parallel$ and $A_\perp$, they are shown in table 2 divided by the Reynolds number, Re, to allow a direct comparison to be made with $\overline{R_\parallel}^{1/2}$ and $\overline{R_\perp}^{1/2}$, and $\Delta_\parallel^{1/2}$ and $\Delta_\perp^{1/2}$. This shows that the mean-squared temporal velocity fluctuations, over the range of Reynolds numbers 32–83, are in the range of 0.07–0.27 times the spatially averaged velocity, whereas the temporal fluctuations in the spatially averaged velocity are much smaller, falling in the range 0.0023–0.012 times the spatially averaged velocity. In fact, the intensity of the fluctuations in the spatially averaged velocity, relative to the mean, decrease with increasing Reynolds number, whereas those of the local temporal velocity fluctuations increase monotonically.

As indicated by the square roots of $\overline{R_\parallel}$ and $\overline{R_\perp}$ in table 2, the velocity variance does not depend very much on the Reynolds number when it is scaled with the spatially averaged velocity. This indicates that the topology of the time-averaged velocity field does not change significantly with increasing Reynolds number. In contrast, the temporal velocity fluctuations, which are quantified by the square roots of $\Delta_\parallel$ and $\Delta_\perp$ in table 2, increase significantly with the Reynolds number.

At all the Reynolds numbers considered here, the time-averaged variance of the streamwise component of the velocity is approximately twice that of each of the cross-stream components. However, the temporal velocity fluctuations in the streamwise and cross-stream directions are comparable at a Reynolds number of 83, whereas at smaller Reynolds numbers, when the fluctuations are periodic, the temporal fluctu-

ations in the streamwise direction are considerably larger than those in the cross-stream directions. This tendency for the fluctuating kinetic energy to be distributed equally in all directions with increasing Reynolds number is consistent with what is expected in turbulent flows at very large Reynolds numbers, i.e. at the smallest scales of a turbulent flow the velocity fluctuations are isotropic and independent of the large-scale 'structures', which are typically anisotropic.

In turbulent flows, the rate at which the kinetic energy of the largest (inertial) scales is dissipated at the smallest (viscous) scales defines the so-called Kolmogorov length, time and velocity microscales. These are given by $\ell = (\nu^3/\epsilon)^{1/4}$, $\tau = (\nu/\epsilon)^{1/2}$ and $\upsilon = (\nu\epsilon)^{1/4}$, respectively, where ϵ is the rate of viscous dissipation (per unit mass), which is equal to the rate at which the fluctuating kinetic energy is produced at the largest scales. If the velocity fluctuations at the largest scales are taken to be $(Re\,\nu/a)(\Delta_\parallel + 2\Delta_\perp)^{1/2}/\sqrt{3}$, and the characteristic time scale for these fluctuations is assumed to be ω_1^{-1}, then

$$\epsilon \sim (Re\,\nu/a)^2(\Delta_\parallel + 2\Delta_\perp)/3\omega_1. \tag{19}$$

The fundamental frequency, ω_1, may be obtained from (9). Substituting the approximation for ϵ in (19) into the scaling relationships for the microscales given above, and using the simulation results in table 2 for a Reynolds number of 83.0 and a sphere radius of 31.8 lattice units, gives $\ell \sim 1.26$ lattice units, $\tau \sim 160$ time steps, and $\upsilon \sim 8.0 \times 10^{-3}$ lattice units per time step. This simple analysis helps confirm that the spatial and temporal resolution of the simulations with a sphere radius of 31.8 lattice units, and hence also those with a sphere radius of 48.8 lattice units, is sufficient to resolve the smallest length and time scales that could be expected at such a Reynolds number. The non-dimensional frequency corresponding to the dissipative time scale seems reasonable, since, at this Reynolds number, the Fourier spectra in figure 7(*d*) show that most of the energy is in modes whose frequencies are less than approximately $600\nu/a^2$.

At a Reynolds number of approximately 32, the temporal evolution of the velocity variance in figure 18 shows that the velocity fluctuations in the cross-stream direction closely follow the changes in the spatially averaged velocity. However, the velocity fluctuations in the streamwise direction lead by approximately one-third of a period. Therefore, at this relatively small Reynolds number, inertia mostly affects the coupling between the streamwise velocity fluctuations and the spatially averaged velocity, whereas the dynamics of the cross-stream velocity fluctuations are viscous and quasi-steady. Another way of interpreting these dynamics is to consider the spatially averaged velocity as responding to the streamwise velocity fluctuations. Then, the increase (decrease) in the streamwise velocity variance can be thought of extracting (releasing) energy from (to) the spatially averaged velocity, which lags by approximately one-third of a period because of its inertia. Again, the cross-stream velocity fluctuations respond almost instantaneously to the spatially averaged velocity.

As shown in figure 19, at a larger Reynolds number of approximately 46, the variance of the cross-stream velocity fluctuations develops a mode whose frequency is twice the fundamental frequency. The higher frequency harmonic allows the variance of the cross-stream velocity fluctuations to alternate between following the spatially averaged velocity, when the spatially averaged velocity decreases, and the streamwise velocity fluctuations, when the variance of the streamwise velocity fluctuations increases. This demonstrates the increasing role that inertia plays in the cross-stream direction, and explains the origin of the higher frequency harmonics observed in the

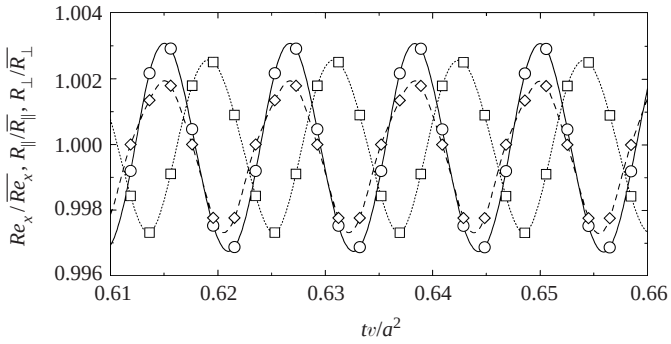

FIGURE 18. Time series of the streamwise component of the spatially averaged velocity, non-dimensionalized with v/a to give a Reynolds number (circles), and the variances of the streamwise (squares) and cross-stream (diamonds) components of the velocity divided by the square of the streamwise component of the spatially averaged velocity. To show their relative phases, the time series have been divided by their respective time-averaged values. These results are from lattice-Boltzmann simulations with $(Re, a, c) = (32.3, 31.8, 0.739)$, where a is in lattice units. The data points identified with symbols are interpolated with splines.

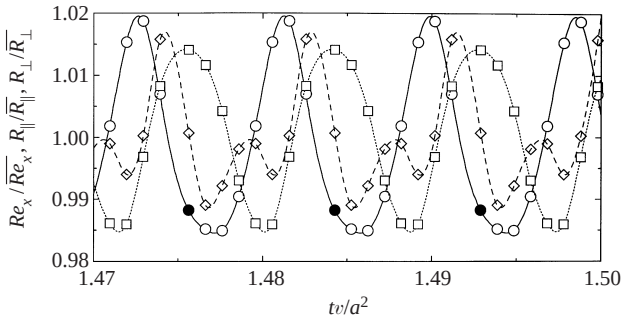

FIGURE 19. The same as in figure 18, but with a larger Reynolds number of 45.9. The time between each data point identified with symbols corresponds to the time separating each projection of the velocity field shown in figures 11 and 13 – the filled circles identify the first image in the sequence.

Fourier spectra of the fluctuating spatially averaged velocity in § 4.2. Note that the fluctuations in the variance of the streamwise component of the velocity are qualitatively similar to those at a Reynolds number of 32. This reflects that, at these relatively small Reynolds numbers, the dynamics of the streamwise velocity fluctuations are dominated by inertia and are independent of the fluctuations in the cross-stream directions.

8. Velocity, vorticity and helicity statistics

In this section, the vorticity, $\boldsymbol{\omega} = \nabla \times \boldsymbol{u}$, and the quantity $\boldsymbol{\omega} \cdot \boldsymbol{u}$, which when integrated over the entire volume of fluid is referred to in the context of turbulent flows as the helicity (Frisch 1995), will be examined. In this work, $\boldsymbol{\omega} \cdot \boldsymbol{u}$, rather than its integral, will be referred to as the helicity.

Similarly to the velocity, the vorticity is considered as the sum

$$\boldsymbol{\omega}(t) = \Omega(t) + \boldsymbol{\omega}'(\boldsymbol{x}, t), \tag{20}$$

where Ω is the spatially averaged vorticity. The variance of the vorticity, non-dimensionalized with the magnitude of the spatially averaged velocity and the sphere

radius, is

$$\boldsymbol{O}(t) = \langle \boldsymbol{\omega}'\boldsymbol{\omega}' \rangle a^2/|\boldsymbol{U}|^2, \tag{21}$$

where the angled brackets indicate the spatial average, which includes the space occupied by the spheres. The variance of the streamwise and cross-stream components of the vorticity are given by the diagonal components of $\boldsymbol{O}$, which will be referred to as

$$O_{\parallel} = O_{xx} \quad \text{and} \quad O_{\perp} = (O_{yy} + O_{zz})/2, \tag{22}$$

respectively. The vorticity was obtained by differentiating the velocity fields using central finite-difference approximations.

In any two-dimensional flow, the helicity is identically zero because the vorticity is perpendicular to the velocity. Since the flow close to the sphere surfaces can be approximated as a simple shear flow, the helicity there may be expected to be small provided that the vorticity is not too large. However, when the flow is three-dimensional, i.e. away from the surfaces of the spheres, the vorticity and velocity may become much more closely aligned, in which case the streamlines tend to have helical trajectories. This motivates examining the cosine of the angle between the vorticity and the velocity,

$$\cos\phi = \frac{\boldsymbol{\omega} \cdot \boldsymbol{u}}{|\boldsymbol{\omega}||\boldsymbol{u}|}. \tag{23}$$

The variance of the helicity, non-dimensionalized with the magnitude of the spatially averaged velocity and the sphere radius, is given by

$$H(t) = [\langle (\boldsymbol{\omega} \cdot \boldsymbol{u})^2 \rangle - \langle \boldsymbol{\omega} \cdot \boldsymbol{u} \rangle^2] a^2/|\boldsymbol{U}|^4, \tag{24}$$

and the variance of the cosine of the angle between the vorticity and velocity is given by

$$C(t) = \langle \cos^2\phi \rangle - \langle \cos\phi \rangle^2, \tag{25}$$

where, again, the angled brackets indicate spatial averages. Note that the helicity is a quantity that is not invariant to a Galilean transformation, and hence it depends on the average velocity. Nevertheless, it provides a useful means of quantifying the geometrical structure of the flows.

The PDFs of a quantity α, say, given by $P(\alpha)$, were obtained by sampling only the space occupied by the fluid. They have been normalized so their standard deviations and $\int_{-\infty}^{+\infty} P(\alpha)\,\mathrm{d}\alpha$ equal one, allowing them to be easily compared to normalized Gaussian and (double) exponential distribution functions. Note that the variance of α over the region occupied by the fluid, $\langle \alpha'^2 \rangle_1$, is related to the variance over the entire domain by

$$\langle \alpha'^2 \rangle_1 = \langle \alpha'^2 \rangle/(1-c) - c\langle \alpha \rangle/(1-c)^2, \tag{26}$$

where $\alpha' = \alpha - \langle \alpha \rangle/(1-c)$, and the angled brackets indicate spatial averages.

Statistics that may be used to scale the normalized PDFs shown below are listed in table 3. Also shown, for reference, and to be consistent with the convention adopted in previous sections, are statistics from the entire domain. Of course, these are related via (26). Note that the variances have been non-dimensionalized with the spatially averaged velocity corresponding to the domain of interest.

In the following discussion, the statistics in table 3 will be referred to in conjunction with selected PDFs when necessary. The results in table 3 are from: (i) simulations of two steady flows with nominal Reynolds numbers of zero and 25; (ii) three time steps from a simulation whose velocity undergoes periodic temporal fluctuations at a

$t'\omega_1$	$4f$	Re	$R_\parallel$	$R_\perp$	$O_\parallel$	$O_\perp$	H	C
(steady)	1.0	0.0132	4.33	2.34	293	447	29.2	0.00142
		0.510	0.380	0.606	75.9	116	0.507	0.0548
(steady)	3000	25.4	4.57	2.30	495	600	7230	0.0550
		98.1	0.443	0.596	128	155	126	0.212
0	7000	44.8	4.65	2.47	734	729	20 700	0.0733
		173	0.463	0.640	190	189	360	0.283
0.306	7000	45.4	4.54	2.46	650	673	15 100	0.0656
		175	0.435	0.637	168	174	262	0.253
0.612	7000	46.7	4.54	2.44	638	677	13 400	0.0641
		180	0.435	0.632	165	175	233	0.247
(chaotic)	29 000	107	4.86	2.55	1040	1020	38 100	0.0812
		413	0.518	0.660	269	264	662	0.314

TABLE 3. Statistics from selected lattice-Boltzmann simulations with $(a, c) = (48.8, 0.741)$, where a is in lattice units. Statistics on odd lines are from the entire computational domain, whereas those on even lines are from the region occupied by fluid. Note that t' is the time relative to that of the realization with $t' = 0$.

nominal Reynolds number of 45; and (iii) a single time step from a simulation whose velocity undergoes chaotic temporal fluctuations at a nominal Reynolds number of 110. The second line of data for each case corresponds to statistics obtained from only the region occupied by the fluid; these are the values that will be referred to in the following discussion, and which were used to scale the abscissae of the normalized PDFs shown below. The Reynolds numbers will still be referred to based on the velocity averaged over the entire domain.

8.1. *Velocity*

The variances of the streamwise and cross-stream components of the velocity do not change significantly with increasing Reynolds number. This might be expected, since the largest contribution to the velocity variance in closely packed arrays of spheres comes from the fluid having to flow along tortuous trajectories close to the solid surfaces. The variance of the streamwise component of the velocity in the region occupied by the fluid is actually smaller than that of the cross-stream components, whereas over the entire domain it is larger. As suggested by (26), this qualitative difference is because of the contribution from the spatially averaged streamwise velocity.

The PDFs of the velocity shown in figures 20 and 21 are from the simulations with nominal Reynolds numbers of 25 and 110, respectively. The PDFs are similar when they are normalized with their respective standard deviations, but not to the same extent as those obtained by Kutsovsky *et al.* (1996) at Reynolds numbers in the approximate range 2.6–8.1. Clearly then, over a relatively large range of Reynolds numbers, the topology is sufficiently different to change the details of the velocity PDFs, but not enough to be detected in the variances of the velocity fluctuations. At larger Reynolds numbers, there is a significantly larger portion of the fluid whose streamwise velocity is directed upstream. These regions are not only because of recirculating flow attached to the downstream faces of the spheres, but also because of vortices whose axes have a component perpendicular to the x-axis. The largest differences occur in the streamwise components of the velocity, particularly the

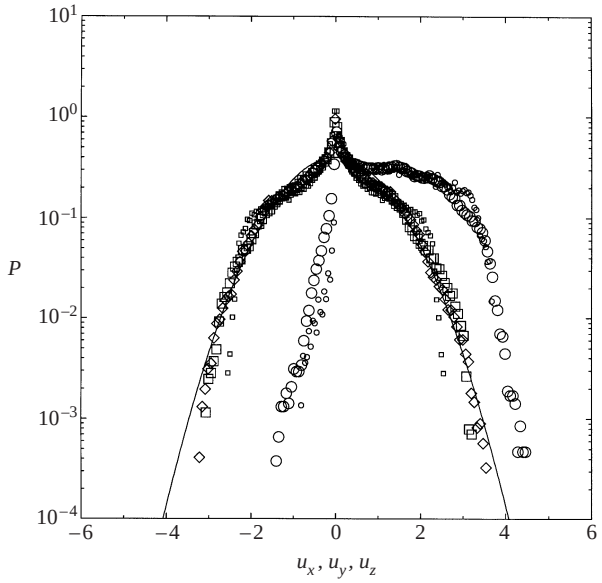

FIGURE 20. Normalized probability distribution functions, at a single instant in time, of the x- (circles) y- (squares) and z- (diamonds) components of the fluid velocity obtained from lattice-Boltzmann simulations with $(a, c) = (48.8, 0.741)$, where a is in lattice units. The small symbols correspond to steady flow with a Reynolds number of 25.4, and the large symbols correspond to unsteady flow with a Reynolds number of 106. The line is a Gaussian distribution with zero mean and a standard deviation of one. Note that the PDFs for the y- and z-components are identical when the flow is steady, and hence only the PDF for the y-component is shown.

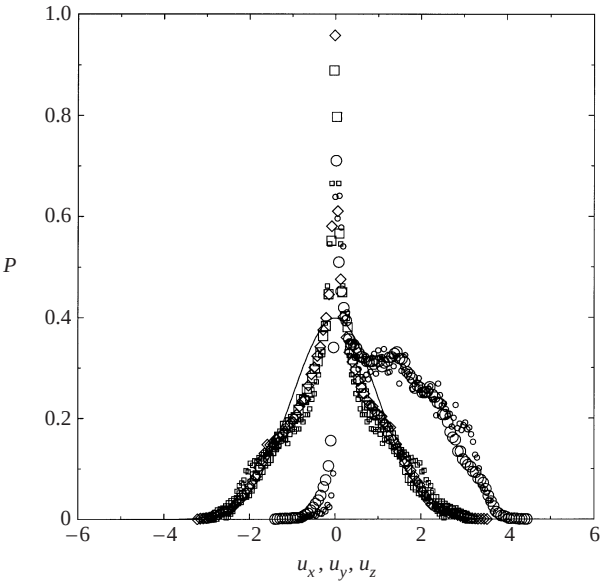

FIGURE 21. The same data as in figure 20, but with the axes scaled to show more clearly the PDFs at small velocities.

contribution from the fluid moving slowly upstream. The tails of the PDFs decay more rapidly than the Gaussian distribution shown for comparison, although the tails of the PDFs of the two cross-stream components of the velocity appear to approach the Gaussian distribution at the largest Reynolds number when the flow

undergoes large-amplitude chaotic fluctuations. These results support the suggestion by Kutsovsky *et al.* (1996) that the exponentially decaying tails observed for flows in randomly packed beds is because of the distribution of pore sizes, rather than the distribution of velocities found within an individual pore. This seems reasonable when considering that the average drag force on the spheres in randomly packed beds – given by the Ergun correlation, for example (Hill *et al.* 2001*b*) – is very sensitive to the solid volume fraction, and hence small variations in the local porosity give rise to large variations in the local fluid velocity. Note that PDFs of the velocity at various times throughout the fundamental period of the unsteady flow whose Reynolds number is 45 are qualitatively the same as those shown here, at a single instant in time, at a nominal Reynolds number of 110.

8.2. *Vorticity*

In contrast to the variance of the velocity, the variance of the streamwise and cross-stream components of the vorticity increases monotonically with increasing Reynolds number. The variance of the streamwise component of the vorticity increases approximately linearly with the Reynolds number. When the flow is steady, the variance of the cross-stream components of the vorticity is significantly larger than that of the streamwise component. With the onset of unsteady flow, however, all the components are approximately equal. This is presumably because of vortex stretching. Without vortex stretching, vorticity is produced by shear flow at the solid surfaces, contributing mostly to the cross-stream vorticity. This is confirmed by the variances of the vorticity shown in table 3 for Stokes flow.

The PDFs of the vorticity shown in figures 22 and 23 are from three time steps of a simulation whose Reynolds number is 45. Similarly to the velocity, the PDFs of the streamwise components are qualitatively different from those of the cross-stream components. At values less than approximately three standard deviations from the mean, the PDFs of the cross-stream components of the vorticity decay exponentially and do not vary much with time. This is because the cross-stream components of the vorticity come from the region of the flow close to the surfaces where the temporal fluctuations in the velocity are relatively small. The PDFs of the streamwise component of the vorticity undergo much larger temporal fluctuations. These fluctuations are not confined to the tails of the distributions, since the large-amplitude velocity fluctuations presumably contribute to both large and small values of the streamwise vorticity.

8.3. *Helicity*

Even more sensitive to the Reynolds number is the variance of the cosine of the angle between the vorticity and the velocity. It increases by a factor of approximately five over the range of Reynolds numbers from zero to the onset of unsteady flow, beyond which it remains approximately constant. Figure 24 shows PDFs of $\cos\phi$ from the simulations with nominal Reynolds numbers of 25 and 110. These show that, with increasing Reynolds number, the portion of the fluid whose vorticity is aligned with the velocity increases significantly. This supports the mechanism by which kinetic energy in the fluctuating spatially averaged velocity is transferred to velocity fluctuations at smaller scales by generating helical vortices. It is interesting to note that the PDF of $\cos\phi$ is the only one of those examined here to change significantly (qualitatively) with the Reynolds number and, indeed, with the fluctuating spatially averaged velocity. The PDFs of $\cos\phi$ are periodic in ϕ, and hence the abscissae have not been scaled with the standard deviation. Although not shown here, the PDF

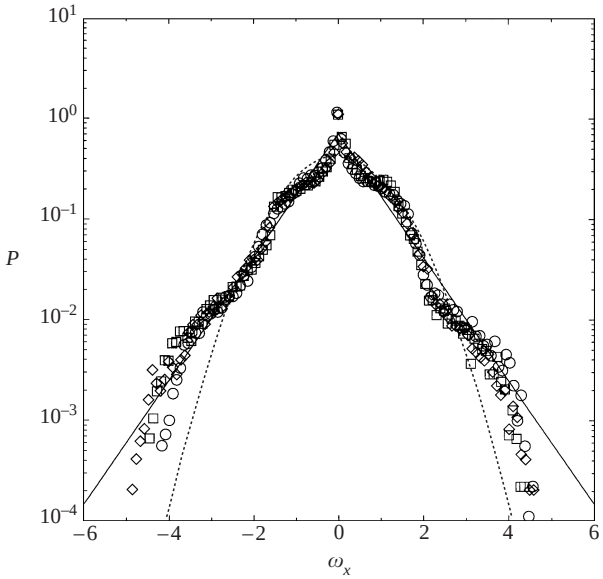

FIGURE 22. Normalized probability distribution functions of the x-component of the vorticity obtained from lattice-Boltzmann simulations with $(Re, a, c) = (45.7, 48.8, 0.741)$, where a is in lattice units. At this Reynolds number, the flow is periodic with a fundamental frequency $\omega_1 = 122v/a^2$. The circles, squares and diamonds correspond to three equally spaced instants in time that span approximately half the fundamental period of the oscillations. The lines are double exponential (solid) and Gaussian (dotted) distributions with zero mean and a standard deviation of one.

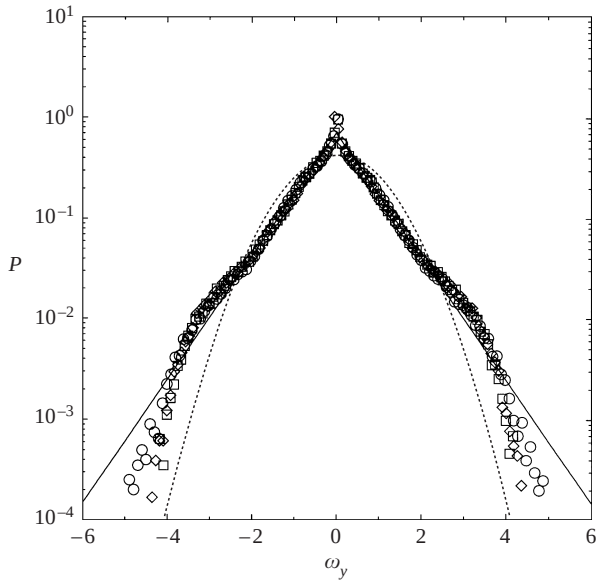

FIGURE 23. As figure 22 but for the y-component of the vorticity.

of $\cos\phi$ for Stokes flow rapidly decays to zero when $\cos\phi \sim 0.2$, and the peak at $\cos\phi = 0$ is approximately 16. Clearly then, the contribution to the PDFs at absolute values of $\cos\phi$ greater than approximately 0.2 is entirely due to the effects of fluid inertia. Note that the PDF of $\cos\phi$ close to $\cos\phi = 0$ and, indeed, the height of

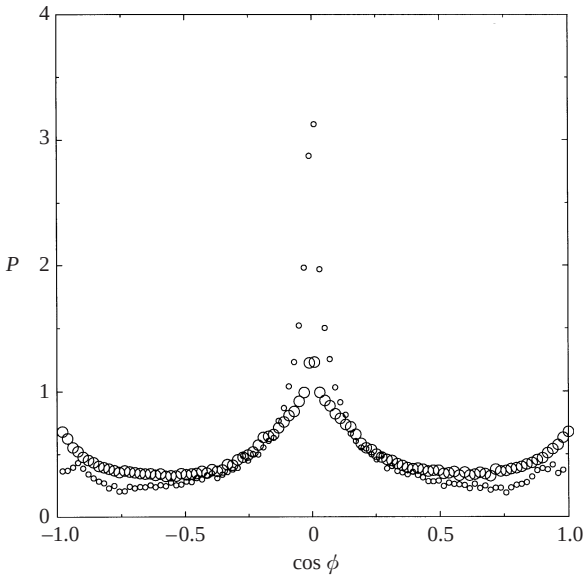

FIGURE 24. Normalized probability distribution function, at a single instant in time, of the cosine of the angle between the velocity and the vorticity obtained from lattice-Boltzmann simulations with $(a, c) = (48.8, 0.741)$, where a is in lattice units. The small symbols correspond to steady flow with a Reynolds number of 25.4, and the large symbols correspond to unsteady flow with a Reynolds number of 106.

the peak at $\cos\phi = 0$ do not fluctuate. This suggests that the velocity field does not change significantly in those regions close to the spheres where the velocity and vorticity are perpendicular to one another. Furthermore, the magnitude of the peak at $\cos\phi = 0$ is between those shown at smaller and larger Reynolds numbers in figure 24, suggesting that at large Reynolds numbers the fluid in the outer region of the flow penetrates further into the shear-dominated flow close to the spheres.

At a nominal Reynolds number of 45, when the temporal fluctuations are periodic, the variance of $\cos\phi$ does not change significantly, but the PDFs in figure 25 show that there are significant changes near $\cos\phi = \pm 1$. These can be explained by the alternating sign of the streamwise vorticity, which, recall, was identified from the projections of the velocity field shown in figure 13. The symmetries that the flow adopts, at least in the case where there are periodic temporal fluctuations, necessitate that the net vorticity be directed at all times along the x-axis, which, together with the changing sign, gives rise to an exchange of probability between angles close to zero and π, or between $\cos\phi = 1$ and -1, respectively.

As the PDFs in figure 26 show, the helicity, which combines the vorticity and velocity, is exponentially distributed. Furthermore, in contrast to the PDFs of the velocity and vorticity, the PDFs of the helicity undergo relatively large temporal fluctuations over a large range of the abscissa. Since the PDFs of the velocity and vorticity do not undergo such significant changes, this behaviour suggests that the fluctuations are because of the fluctuating angle between the vorticity and velocity. Indeed, the PDFs of the cosine of the angle between the velocity and vorticity undergo significant temporal fluctuations, particularly in the tails, since the largest contribution to the PDFs coming from $\cos\phi$ near zero is from the small-amplitude fluctuations in the shear flow close to the solid surfaces.

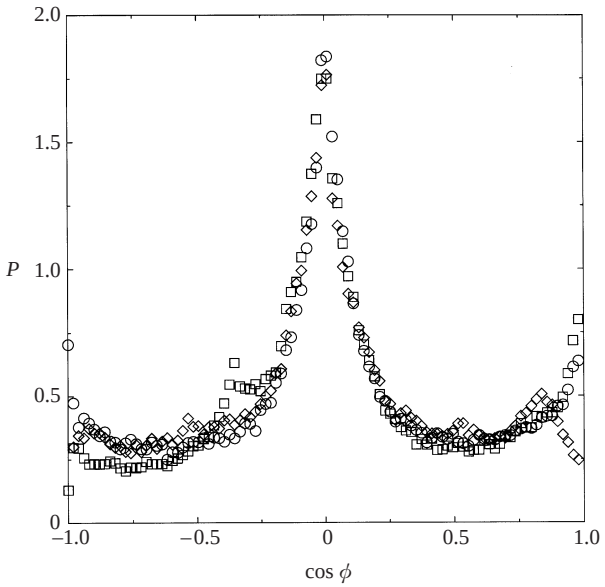

FIGURE 25. Normalized probability distribution functions of the cosine of the angle between the velocity and the vorticity obtained from lattice-Boltzmann simulations with $(Re, a, c) = (45.7, 48.8, 0.741)$, where a is in lattice units. At this Reynolds number, the flow is periodic with a fundamental frequency $\omega_1 = 122\nu/a^2$. The circles, squares and diamonds correspond to three equally spaced instants in time that span approximately half the fundamental period of the oscillations.

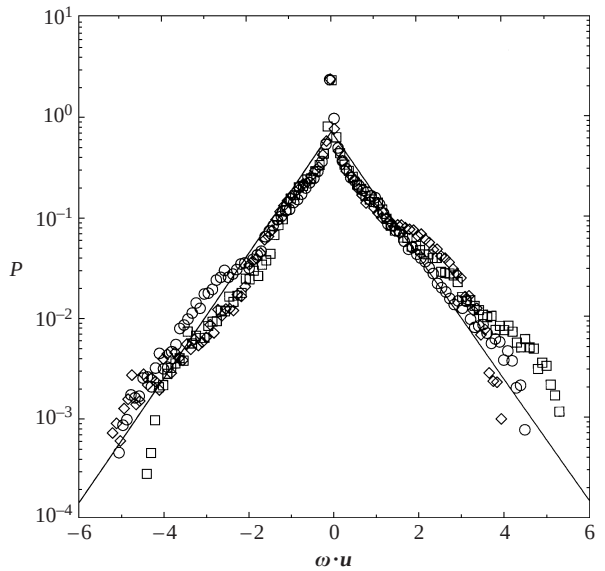

FIGURE 26. As figure 25 but for the helicity.

8.4. *Statistics in a fluid sub-domain*

All the statistics discussed above were obtained from the entire domain occupied by the fluid, and, hence, they were significantly influenced by the regions close to the sphere surfaces. This resulted in characteristic peaks in the velocity PDFs at low

velocities, for example. The PDFs of the cosine of the angle between the velocity and vorticity were also dominated by the contribution from the shear flow close to the sphere surfaces. To briefly examine to what extent the fluid close to the spheres affects the statistics, the velocity, vorticity, helicity and $\cos\phi$ were sampled only in a cubic sub-domain, centred at the origin, occupied only by the fluid (see figure 1). These statistics are compared to those from the entire domain in table 4. In both cases, the results are non-dimensionalized with the spatially averaged velocity on the respective domain, and therefore some care must be taken when comparing the results.

These statistics are from simulations with a sphere radius of 31.8 lattice units, and hence their absolute values may not be as accurate as those in table 3 from simulations with a sphere radius of 48.8 lattice units. For this reason, statistics from a steady flow whose nominal Reynolds number is 25 are also shown. These may be compared directly with the statistics in table 3 from simulations with the same nominal Reynolds number, but with a larger sphere radius of 48.8 lattice units. In general, with the notable exception of the vorticity and helicity statistics, the results are in good agreement. The ratio of the variance of the streamwise vorticity to that of the cross-stream vorticity are within 6% of each other, suggesting that the results are sufficiently accurate for at least qualitative comparisons.

The temporal variations are all relatively small, and hence it is sufficient to focus only on the results at one instant. The spatially averaged velocity in the sub-domain is approximately four times larger than when averaged over the entire domain. This is almost entirely because the average does not include the large volume occupied by the spheres. The spatial velocity variance is considerably smaller, relative to the square of the spatially averaged velocity, and the fluctuations are much more isotropic, but, nevertheless, they are still larger in the streamwise direction than in the cross-stream directions. In contrast, the spatial variance of the streamwise component of the vorticity is larger – by a factor of approximately two – than the two cross-stream components. When sampling the entire domain, the vorticity is dominated by the contribution from the shear flow at the sphere surfaces where the vorticity is mostly perpendicular to the streamlines and, hence, directed predominantly in the cross-stream directions. The apparently large difference in the variances of the helicity is more difficult to interpret. If the variance of the helicity is instead scaled with the product of the mean-squared vorticity and the square of the spatially averaged velocity, then the non-dimensional variances of the helicity, for both the cubic sub-domain and the entire region occupied by the fluid, are within 5% of each other, instead of the approximately 50% differences shown in table 4.

9. Summary

The sequence of transitions in going from steady to chaotic unsteady flow in a close-packed face-centred cubic array of spheres has been examined using lattice-Boltzmann simulations. All the simulations were performed with the average pressure gradient directed along the primary axis of symmetry of the array.

At Reynolds numbers where the flow is steady, the velocity field has the same symmetries as the underlying geometry. At a Reynolds number of approximately 30, the transition to unsteady flow occurs via a supercritical Hopf bifurcation in which only the streamwise component of the spatially averaged velocity fluctuates. The transition to unsteady flow is accompanied by a breaking of rotational symmetry, resulting from the development of a vortex at the centre of the domain whose axis is aligned with the flow and whose direction of rotation alternates with the fundamental frequency.

t'	$4f$	Re	$R_\parallel$	$R_\perp$	$O_\parallel$	$O_\perp$	H	C
0	19 000	82.4	4.71	2.27	685	732	25 300	0.0771
		310	0.519	0.604	182	195	476	0.290
		325	0.557	0.404	161	88.1	293	0.358
50	19 000	82.3	4.68	2.33	716	728	27 600	0.0800
		309	0.511	0.620	190	194	519	0.301
		328	0.537	0.418	164	86.7	318	0.379
100	19 000	82.7	4.61	2.35	718	721	28 200	0.0805
		311	0.492	0.625	191	192	531	0.303
		332	0.488	0.426	163	81.5	291	0.375
150	19 000	82.8	4.56	2.39	720	713	27 300	0.0783
		311	0.479	0.636	192	190	514	0.294
		336	0.464	0.423	159	79.0	265	0.363
(steady)	3000	25.9	4.46	2.19	400	514	6810	0.0513
		97.4	0.452	0.583	106	137	128	0.193

TABLE 4. Statistics from selected lattice-Boltzmann simulations with $(a, c) = (31.8, 0.734)$, where a is in lattice units. Statistics on the first line at each time are from the entire computational domain, those on the second line are from the entire region occupied by the fluid, and those on the third are from a cubic sub-domain (centred at the origin) occupied only by fluid. Note that t' is the time relative to that of the realization with $t' = 0$.

At a Reynolds number of approximately 50, a further symmetry-breaking bifurcation occurs, giving rise to quasi-periodic fluctuations with three fundamental frequencies. Symmetry breaking is accompanied by the onset of fluctuations in all three components of the spatially averaged velocity. In this case, the dynamics of the two cross-stream components of the spatially averaged velocity are different. At an only slightly larger Reynolds number, the Fourier spectra become continuous, indicating the onset of chaotic dynamics. Then, with increasing Reynolds number, the temporal velocity fluctuations become increasingly isotropic.

The probability distribution functions of the velocity, vorticity and helicity, and visualizations of the unsteady flows in various dynamic states, show that vortices are produced in which the velocity and vorticity are closely aligned with one another. With increasing Reynolds number, the geometrical structure of the flow changes from one that is dominated by extension and simple shear to one in which the streamlines are helical. A mechanism for the dynamics was proposed in which energy is transferred to smaller scales by the dynamic interaction of vortices sustained by the underlying time-averaged flow.

The distribution of the angle between the velocity and vorticity was shown to be a quantity that depends very much on the Reynolds number and undergoes significant temporal fluctuations. The PDFs of the velocity and vorticity, however, do not change significantly with the Reynolds number when the abscissae are scaled with their respective standard deviations. The tails of the velocity PDFs decay slightly faster than Gaussian distributions, but approach Gaussian distributions at the largest Reynolds numbers.

This computational study goes some way toward characterizing turbulent flows in porous media, particularly at the relatively small Reynolds numbers where the transition occurs. The geometrical characteristics of the simulated steady flows are in agreement with experimental observations reported in the literature. As yet, however,

there are no quantitative experimental studies examining the dynamics of such flows. Indeed, it would be an interesting and challenging task to make such a comparison. The length and time scales of the flows reported here should assist in the design of such an experiment. The physical mechanisms revealed by these simulations will also hopefully contribute toward the development of models for moderate-Reynolds-number flow, dispersion, and mixing in porous media.

This work was funded by the National Science Foundation (NSF) and the National Aeronautics and Space Administration (NASA) under grant numbers CTS-9526149 and NAG3-2440, respectively. The computations were performed using the resources of the Cornell Theory Center. We would also like to thank Anthony J. C. Ladd for providing the lattice-Boltzmann code, and Olus Boratav (Cornell University) and Andrew Reynolds (Silsoe Research Institute) for helpful discussions.

REFERENCES

Dybbs, A. & Edwards, R. V. 1984 A new look at porous media fluid mechanics – Darcy to turbulent. In *Fundamentals of Transport Phenomena in Porous Media* (ed. J. Bear & M. Y. Corapcioglu), pp. 199–254. Martinus Nijhoff.

Frisch, U. 1995 *Turbulence*. Cambridge University Press.

Ghaddar, C. K. 1995 On the permeability of unidirectional fibrous media: a parallel computational approach. *Phys. Fluids* **7**, 2563–2586.

Hill, R. J. 2001 The effects of fluid inertia on flows in porous media. PhD thesis, Cornell University.

Hill, R. J. & Koch, D. L. 2002 Moderate-Reynolds-number flow in a wall-bounded porous medium. *J. Fluid Mech.* **453**, 315–344.

Hill, R. J., Koch, D. L. & Ladd, A. J. C. 2001*a* The first effects of fluid inertia on flows in ordered and random arrays of spheres. *J. Fluid Mech.* **448**, 213–241.

Hill, R. J., Koch, D. L. & Ladd, A. J. C. 2001*b* Moderate-Reynolds-number flows in ordered and random arrays of spheres. *J. Fluid Mech.* **448**, 243–278.

Hinze, J. O. 1987 *Turbulence*. McGraw-Hill.

Jolls, K. R. & Hanratty, T. J. 1966 Transition to turbulence for flow through a dumped bed of spheres. *Chem. Engng Sci.* **21**, 1185–1190.

Karabelas, A. J., Wegner, T. H. & Hanratty, T. J. 1973 Flow pattern in a close packed cubic array of spheres near the critical Reynolds number. *Chem. Engng Sci.* **28**, 673–682.

Kaviany, M. 1995 *Principles of Heat Transfer in Porous Media*. Springer.

Koch, D. L. & Ladd, A. J. C. 1997 Moderate Reynolds number flows through periodic and random arrays of aligned cylinders. *J. Fluid Mech.* **349**, 31–66.

Kutsovsky, Y. E., Scriven, L. E., Davis, H. T. & Hammer, B. E. 1996 NMR imaging of velocity profiles and velocity distributions in bead packs. *Phys. Fluids* **8**, 863–871.

Ladd, A. J. C. 1994*a* Numerical simulations of particulate suspension via a discretized Boltzmann equation. Part 1. Theoretical foundation. *J. Fluid Mech.* **271**, 285–309.

Ladd, A. J. C. 1994*b* Numerical simulations of particulate suspension via a discretized Boltzmann equation. Part 2. Numerical results. *J. Fluid Mech.* **271**, 311–339.

Lahbabi, A. & Chang, S. C. 1985 High Reynolds number flow through cubic arrays of spheres. *Chem. Engng Sci.* **40**, 435–447.

Lebon, L., Oger, L., Leblond, J., Hulin, J. P., Martys, N. S. & Schwartz, L. M. 1996 Pulsed gradient NMR measurements and numerical simulation of flow velocity distribution in sphere packings. *Phys. Fluids* **8**, 293–301.

Maier, R. S., Kroll, D. M., Kutovsky, Y. E., Davis, H. T. & Bernard, R. S. 1998 Simulation of flow through bead packs using the lattice-Boltzmann method. *Phys. Fluids* **10**, 60–74.

van der Merwe, D. F. & Gauvin, W. H. 1971 Velocity and turbulence measurements of air flow through a packed bed. *AIChE J.* **17**, 519–528.

Mickley, H. S., Smith, K. A. & Korchak, E. I. 1965 Fluid flow in packed beds. *Chem. Engng Sci.* **20**, 237–246.

Reynolds, A. M., Reavell, S. V. & Harral, B. B. 2000 Flow and dispersion through a close-packed fixed bed of spheres. *Phys. Rev.* E. **62**, 3632–3639.

Tennekes, H. & Lumley, J. H. 1994 *A First Course in Turbulence*. The MIT Press.

Wegner, T. H., Karabelas, A. J. & Hanratty, T. J. 1971 Visual studies of flow in a regular array of spheres. *Chem. Engng Sci.* **26**, 59–63.